**POLITECNICO DI MILANO**

DIPARTIMENTO DI FISICA
Corso di Laurea in Ingegneria Fisica


# Miniature plastic high pressure cell for x-ray spectroscopy in multi-extreme conditions.

**Relatore: Prof. Giacomo Ghiringhelli**

**Correlatore: Dr. Cornelius Strohm**

**Tesi di laurea di:**
**Eric VEZZOLI**
**Matr. 765394**

**Anno Accademico 2011-2012**

*Alla mia famiglia*
*che ha sempre appoggiato le mie scelte*
*e a tutti i miei amici*
*avete fatto di me la persona che sono.*

*E a G.*

**Sommario**

Dalla sua prima osservazione nel 1947 presso i laboratori della General Electric, a New York, la radiazione di sincrotrone é stata sempre più utilizzata dalla comunità scientifica grazie allo sviluppo di strutture capaci di generarla. Grazie alla sua piccola lunghezza d'onda, nell'ordine dei nanometri, consente lo studio della materia su scala atomica, ha un'elevata brillanza e potenza e consente l'acquisizione di dati con risoluzione spaziale, temporale ed energetica. Questa tesi tratta dello sviluppo di un sistema per lo studio in spettroscopia di assorbimento in condizioni estreme di pressione, temperatura e campo magnetico. Tale tecnica studia le proprietà della materia osservando l'andamento del coefficiente di assorbimento in funzione dell'energia della radiazione, il quale é sensibile a composizione, struttura elettronica e magnetismo dei materiali: ciò dona a questa tecnica la peculiarità di essere orbitale ed elemento selettiva. I primi due capitoli del lavoro sono dedicati alla descrizione dei sincrotroni e della radiazione da essi generata accompagnata da una descrizione delle due tecniche di assorbimento presentate XANES - X-ray Absorption Near Edge Structure ed EXAFS - Extended X-ray Absorption Fine Structure. La prima riguarda l'analisi degli spettri di assorbimento intorno al picco e la seconda riguarda invece la regione a più alta energia, fornendo informazioni sia strutturali che elettroniche. Dopo la presentazione delle due tecniche viene presentata la particolare struttura di ID24, che con la sua geometria dispersiva consente l'acquisizione seriale di spettri di durata nell'ordine dei $\mu s$. La beamline ben si presta all'esperimento pianificato in multi-extreme condition: la presenza di un criostato a flusso di $He$ a $1.5K$ ed un magnete impulsato di $30T$ richiedono un aquisizione seriale di spettri per le variabili condizioni di campo magnetico durante l'impulso. In seguito propongo una panoramica sulla fisica degli strongly correlated electron systems, in cui la presenza di orbitali $d-$ o $f-$ non completi comporta l'impossibilità

di spiegare le loro proprietà attraverso un modello ad elettroni non interagenti. L'apparizione di superconduttivtà ad alta temperatura, strane proprietà magnetiche, effetto Kondo ed altre proprietà esotiche non descritte da una teoria classica hanno aumentato l'interesse scientifico per questo genere di composti. In particolare mi soffermerò sugli Heavy Fermion Compound (HFC) per le loro proprietà elettroniche accordabili tramite l'applicazione di pressione, campo magnetico o temperatura. In questi composti appare spesso una fase superconduttiva mediata da interazioni antiferromagnetiche attorno ai Quantum Critical Points (QCP). Per lo sviluppo di una teoria che spieghi in modo esaustivo il comportamento degli HFC a bassa temperatura sono necessari nuovi dati sperimentali. L'assenza di un sistema che coinvolga la presenza di temperature criogeniche, alti campi magnetici ed alte pressioni per la spettroscopia in assorbimento di HFC porta alla prima parte del mio lavoro: lo sviluppo di una cella ad alte pressioni che possa operare in condizioni sperimentali di temperatura criogenica e campi magnetici impulsati. Per progettarla ho svolto numerose simulazioni per definire l'ambiente sperimentale; fatto ciò ho simulato l'evoluzione della temperatura e della forza di un'ipotetica cella metallica amagnetica all'interno del magnete e criostato concludendo che non poteva in alcun modo soddisfare le richieste sperimentali. Questi risultati ci hanno spinto a progettare e realizzare una cella totalmente composta da plastica, basata sul concetto di arridatoio. Dopo la realizzazione ho proceduto alla messa in opera della cella ed alla prova sperimentale, ovvero il cambiamento di colore attorno a $3.5GPa$ di un campione di Crocoite $PbCrO_4$ accoppiato alla variazione di fluorescenza di un rubino dovuta alla pressione. Lo spettro di assorbimento di un foglio di $Cu$ acquisito serialmente durante tutta la durata dell'impulso dimostra l'utilizzabilità dell'intero sistema sperimentale: le vibrazioni indotte dall'interazione del campo magnetico con la struttura corrompono gli spettri solo dopo il termine dell'impulso. Ciò dimostra che per la prima volta é possibile acquisire uno spettro ragionevole con campi magnetici impulsati, temperature criogeniche ed alte pressioni. Dopo la dimostrazione tecnica ho proceedu-

to all'analisi degi spettri in assorbimento di due Heavy Fermion Compound $YbCu_2Si_2$ e $YbRh_2Si_2$ presi su BM23 per mostrare la fluttuazione di valenza in funzione della tempertura. Diversi fenomeni fisici contribuiscono a stabilizzare la presenza degli ioni $Yb^{2+}$ e $Yb^{3+}$ che differiscono di un elettrone nella shell $4f$. Con il lavoro da me svolto la spettroscopia a raggi X in condizione estreme di campi magnetici ($30T$), temperatura ($1.5K$) possono essere combinati con una pressione di ($6GPa$). Questo ha significativamente aumentato lo spazio delle fasi accessibile per lo studio degli strongly correleted electron systems.

# Contents

# Introduction

Since its first observation in 1947 at the General Electric Research Laboratory in New York, synchrotron radiation has been increasingly used by the scientific community thanks to the development of facilities able to exploit this sort of radiation as a tool to investigate the world down to the nanometer and angstrom scale in the universe of atoms and molecules. Third generation synchrotron facilities are dedicated structures to generate intense and directional x-rays and made it possible to exploit the power and brilliance of radiation with spatial, temporal and energy resolution. This thesis focuses on the development of energy dispersive absorption spectroscopy in multi-extreme conditions of temperature pressure and magnetic field. This technique studies material properties by observing X-ray absorption which is sensitive to its composition, local and electronic structure and magnetism. This gives to spectroscopy its peculiar characteristic of being element and orbital selective. The first two chapter of this thesis are dedicated to the properties of synchrotron radiation, the facilities for its generation and exploitation and to an overview of absorption spectroscopy techniques. Different techniques as XANES - X-ray Absorption Near Edge Structure and EXAFS - Extended X-ray Absorption Fine Structure are available to study the absorption of X-rays from materials of different composition. This technique provides information on the matter and electronic structure of materials. After this introduction, the beam line ID24 structure and the set-up for experiment in multi-extreme conditions will be described. A pulsed magnet coupled with a $He$ flow sample cryostat and the particular set-up of ID24 beam line provide time resolved measurements on $ms$ scale in fields up to $30T$ and tempera-

tures down to $1.5K$. The energy-dispersive concept and the high photon flux of this the beam line make it possible to acquire a full spectrum around the absorption edge in microseconds. After this technical introduction, chapter 3 gives an overview on strongly correlated electrons systems. In these solids the presence of unfilled $d-$ or $f-$ electron shells leads to the impossibility to explain the electronic behaviour with a non interacting electron-model. The appearance of high-T superconductivity, strange magnetic properties, Kondo effect and other exotic properties not described by classic theories, has raised interest in these compounds. In particular I will focus on heavy fermion compounds for their ability to have their properties tuned by pressure and magnetic field as well as temperature. The appearance of superconductivity driven by antiferromagnetic fluctuations and the presence of phase transitions determining Quantum Critical Points suggest more studies on this materials. The lacking of a system that can provide high pressure, low temperature and high magnetic field X-ray absorption studies lead to the first part of my work: the development of a miniature high pressure cell for pulsed magnetic field and cryogenic temperature. Detailed simulations on eddy current heating and forces arising from the interaction of the induced currents with the field lead to the conclusion that even a non-magnetic metallic cell could not fit our purpose. We therefore developed a cell of the turnbuckle type made entirely by engineering plastics to fit into the limited sample space inside the cryostat of the pulsed field set-up. In the following we proceed on the design and realization of this new cell and on the laboratory commissioning of it. To demonstrate the performance of the cell I observed the colour change at $3.5GPa$ of a sample of Crocoite $PbCrO_4$ combined with a pressure measurement by the the ruby fluorescence technique. After that the same cell was tested in the multi-extreme condition set-up to demonstrate the operation of the cell for studies through the acquisition of spectra from a Cu foil during the field pulse. After this technical part we show a study of the valence as a function of temperature in the mixed valence compounds $YbCu_2Si2$ and $YbRh_2Si_2$ with spectra taken on BM23. In this Heavy Fermion Compound

(HFC) systems the $14^{th}$ electron of the $4f-$ shell of the $Yb^{2+}$ ion becomes a delocalized and goes into the Fermi sea as a function of the temperature. In these samples the competition of different phenomena leads to the presence of 2 valence states. Through the work carried out during this thesis, X-ray spectroscopy in multi-extreme conditions of field ($30T$), temperature ($1.5K$) can be combined with pressure up to $6GPa$ for the first time. This significantly increase the thermodynamical phase space accessible for the study of strongly correlated electron systems.

# Chapter 1

# Interaction of X-rays with matter

In the common world the visible light is enough for our concept of image, but this is just a small part of the entire electromagnetic spectrum. The interaction between the radiation and the world depends on many factors: intensity, polarization and wavelength. The resolution power of light is related to the latter: the smallest object that the radiation could resolve is related to the wavelength. The visible spectrum ranges approximately from 300 to 800$nm$. Mainly for this reason we can see a human cell, microbes and all bigger object, but not atoms with an optical microscope.

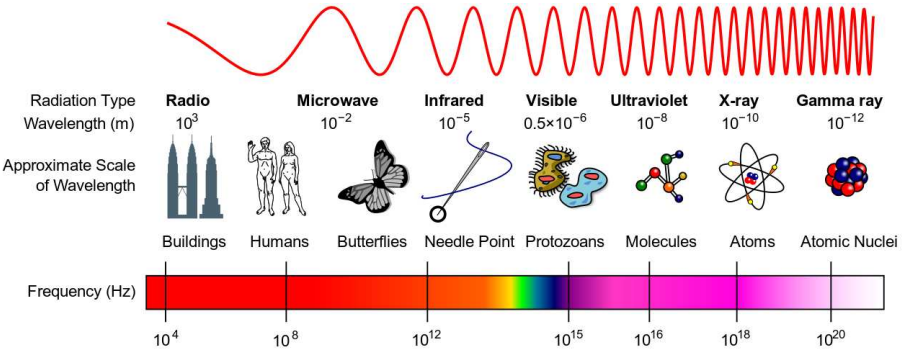


Figure 1.1: electromagnetic spectrum [4]

As we can see in Fig 1.1, to investigate the matter on the atomic scale $10^{-10}m$ one need to use a different portion of the electromagnetic spectrum:

X-rays. The following chapters explain how this radiation can be used to investigate the structure of matter.

## 1.1 Matter interaction

Wilhelm Conrad Röntgen discovered X-rays in 1895, he accidentally put a photographic plate near a tube of inert gas bombarded with electrons at high energy. He realized that the plate had been hit by a sort of unknown radiation, which he named it X-rays. After a while he took an X-ray image of the hand of his wife Fig. 1.2 and realize that different materials adsorb this radiation in differently: soft tissue, mostly composed by water and organic molecules, absorbs less radiation than human bones with an high concentration of calcium. For this discovery he received the first Nobel prize in physics that was awarded in 1901.

Figure 1.2: first X-ray photo made on the human body, the high absorption power of human bones is due to the presence of calcium. The presence of a metal ring can be easily seen in the picture. [4].

From a quantum mechanical point of view, X-rays are photons with energy $E = h\nu$ and momentum $p = \frac{h}{\lambda}$ where $\nu$ is the frequency of the radiation,

$h$ Plank's constant and $\lambda$ the radiation wavelength. The relation between $\lambda$ and $\nu$ is $c = \lambda\nu$ where $c$ is the speed of light. The relation between $\lambda$ in $\mathring{A}$ and $E$ expressed in $keV$ is:

$$\lambda[\mathring{A}] = \frac{hc}{E} = \frac{12.398}{E[keV]} \tag{1.1.1}$$

Depending on the energy of the incoming X-ray, different interactions take place between photons and matter. Radiation between hundreds of eV and MeV is considered to be in the X-ray range. These different interactions can be resumed in a cross section defined as:

$$\frac{d\sigma}{d\Omega} = \frac{I(\phi,\theta)}{I_0} \tag{1.1.2}$$

where $I$ is the photon flux and $I(\phi,\theta)$ the number of events in the solid angle $d\Omega = sin\theta d\theta d\phi$. The total cross section is found by integrating this differential cross section over the solid angle. As it is shown in Fig. 1.3 the main scattering effect is related to the energy that we are interested in. In modern synchrotron facilities it is possible to generate radiation from hundreds of eV to ten thousands of eV. In this region the most important interaction is the photoelectric one, followed by elastic and inelastic scattering.

## 1.2 Photoelectric effect

The idea that radiation is quantized was first proposed by Albert Einstein in 1905: he suggested that the radiation is an ensemble of packages of energy called photons. He used this new concept to explain the photoelectric effect with a simple and elegant picture, for this reason he received the Nobel prize in 1921.

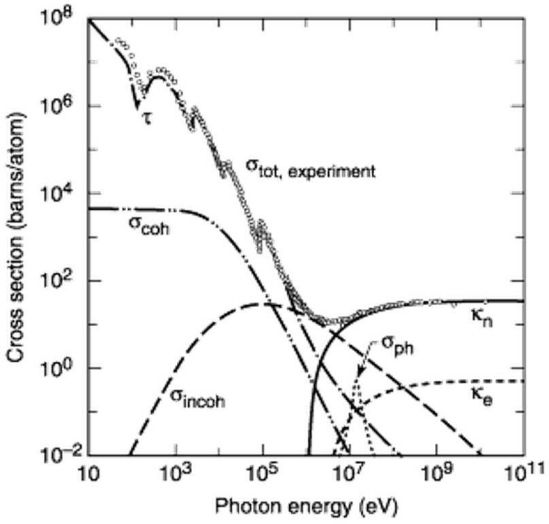


Figure 1.3: energy dependence of the total cross-section for lead. In the picture, the total cross-section is decomposed in various contributions: coherent and incoherent scattering, photoelectric effect and pair production [37].

The theory explains with a simple model, based on the absorption of discrete quanta of light, the features of the phenomenon and its characteristic frequency. Assuming that the radiation is composed by quanta, and that quantum energy decreases with the radiation frequency; the explanation of the sharp threshold in frequency, that appears in the photoelectric effect became simple: only the photons with a certain energy bigger than the electron binding energy could promote a bound electron into the unbound state. The energy of the photo-electron is related to the energy of the incoming photon by:

$$h\nu = h\nu_0 + E_{Kin} + \phi_0 \tag{1.2.1}$$

with $h\nu$ being the energy of the incoming photon, $h\nu_0$ the binding energy of the electron, $\phi_0$ the work function present in solids for the potential energy on the solid's surface and $E_{kin}$ the kinetic energy of the free electron. The electron kinetic energy is the photon energy minus the energy needed to overcome the Fermi level. This simple picture explains really well why even a huge radiation intensity below the electron binding energy can not cause

the photoelectric emission of an electron. From this cornerstone, the theory of matter-radiation interaction was developed in a few years. Fermi proposed his golden rule [34, 56] that allows to estimate the transition probability $\Gamma_{i,f}$ form a first state to a final one, described by the electronic wave functions $|i\rangle$ and $|f\rangle$ respectively interacting with a generic Hamiltonian $H_{int}$:

$$\Gamma_{i,f} = \frac{2\pi}{h^2}|\langle f|H_{int}|i\rangle|^2\delta(h\nu - E_i + E_f) \tag{1.2.2}$$

Where $H_{int}$ represents the electromagnetic field Hamiltonian. This equation governs every electronic transition and every case could be described with it. If we look into the squared part of the eq. (1.2.2) called matrix element M we can write explicitly the Hamiltonian for a resonant transition

$$M \propto \left| \int \psi_f^*(\vec{\epsilon}\cdot\vec{r})e^{i(\vec{k}\cdot\vec{r})}\psi_i d^3x \right|^2 \tag{1.2.3}$$

In the easiest case $H_{int}$ can be treated in the electric dipole approximation: this considers the radiation wavelength bigger than the system that it is interacting with. The field can then be treated as constant on the atomic distance and the exponential term on the plane wave $\left[i(\omega t - \vec{k}\cdot\vec{r})\right]$ can be approximated with 1. In this situation the interaction is reduced to $e\vec{\epsilon}\cdot\vec{r}$ where $e$ is the electron charge, $\vec{\epsilon}$ is the polarization versor of the incident ray and $\vec{r}$ the electron's position coordinate. If we consider then a hydrogen-like wavefunction $\psi$, the selection rule form eq. (1.2.3) becomes $\Delta l = \pm 1$, $\Delta m = 0$ and $\Delta S = 0$. This approximation doesn't take into account effects like spin-orbit coupling, or other perturbations.

This approximation doesn't apply to the case of X-rays. In fact one has to consider the quadrupole transition [35]. In this case the spatially dependent part of $e^{i(\omega t - \vec{k}\cdot\vec{r})}$ is expanded to $1 - \vec{k}\cdot\vec{r}$ and the matrix element has an additional term:

$$M \propto \left| \int \psi_f^* \left[i(\vec{\epsilon}\cdot\vec{r})(\vec{k}\cdot\vec{r})\right] \psi_i d^3x \right|^2 \tag{1.2.4}$$

In this case different selection rule are present: $\Delta l = 0, \pm 2$. This situation make a transition between the state $1s$ to $3d$ possible. The probability of this

transition is much smaller for the dipole transition: transition probabilities for K-edges are smaller by a factor of $(Z\alpha)^2$ with Z the atomic number and $\alpha \sim \frac{1}{137}$ is the fine structure constant. Fig. 1.4 shows a schematic view of a K edge adsorption process.

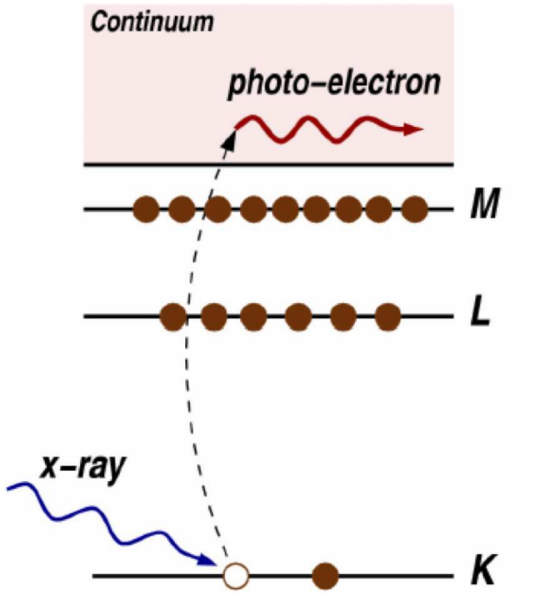


Figure 1.4: interaction between an X-ray and a core electron from a $K$ shell in X-ray absorption. The figure also contains the L and M level with their classic nomenclature. [49]

The nomenclature used in the picture respects the origin of the electron involved. The level with the quantum number $n = 1$ is related to the letter $K$, $n = 2$ in related with $L$ and $n = 3$ with $M$. There is a distinction inside the level $L$ between the suborbital: it's called $L_1$ if it came from level $2s$, $L_2$ if it came from level $2p_{\frac{1}{2}}$ and $L_3$ if it came from level $2p_{\frac{3}{2}}$. The electron involved in absorption can also end up in a unoccupied level just below the ionization energy, this explains the pre edge features in the absorption spectra. As explained in eq. (1.2.1) the energy of a photoelectron is related with the incident photon energy.

## 1.3 XAS: X-ray absorption spectroscopy

XAS - X-ray Absorption Spectroscopy is a technique that measures the absorption coefficient in a sample as a function of the incident photon energy.

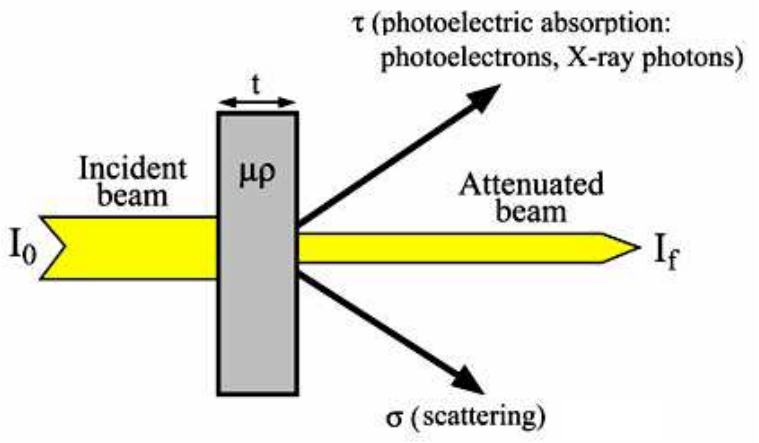


Figure 1.5: Simple representation of an X-ray absorption experiment through a sample of thickness t. In addiction to absorption other processes can be involved in the reduction of the transmitted intensity [4].

A XAS experiment measures the absorption coefficient $\mu(E)$ of a sample, as defined by Lambert-Beer's law:

$$I_f = I_0 e^{\mu(E)t} \tag{1.3.1}$$

where $I_f$ and $I_0$ are the final and initial X-ray intensity and t is the sample thickness. The coefficient $\mu(E)$ varies from material to material, but has some features in common:

1. The absorption coefficient decreases with increasing energy following approximately the relation:

$$\mu(E) = \frac{\rho Z^4}{AE^3} \tag{1.3.2}$$

where $\rho$ is the mass density, Z the atomic number, A the mass number and E the energy. This equation means that the penetration power of an X-ray increases with the energy [25].

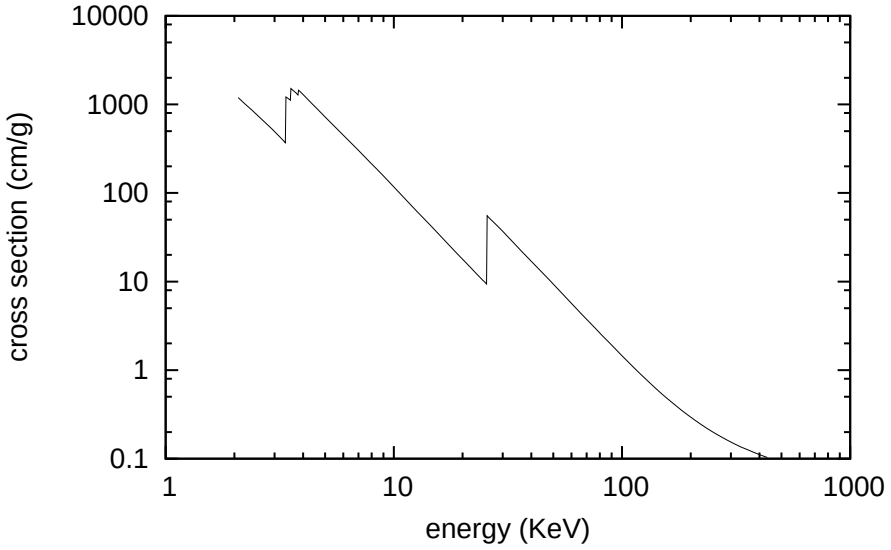


Figure 1.6: cross section of a Silver foil as function of X-ray energy, [21]

2. The discontinuities in Fig. 1.6 correspond to energies that allow to promote a bound electron above the Fermi level, which leads to an increased absorption cross-section. These features, called edges, are different for every material: edges are always roughly at the same energy for a given element.

3. The shape of the absorption edges depend on the physical state of the element: gases have a sharp edge and smooth profile after the edge Fig. 1.7 a, solids and liquids present an oscillating profile around the edge 1.7 b. The oscillating behaviour is due to the scattering of the first shell of neighbours surrounding the absorber atom. The wavelength is related to the energy of the incoming photon through eq. (1.2.1), and scattering from neighbour atoms leads to back scattered waves, that modify the absorption probability. The amplitude of the oscillations contains information on the nature and number of neighbours, and the frequencies on their distance.

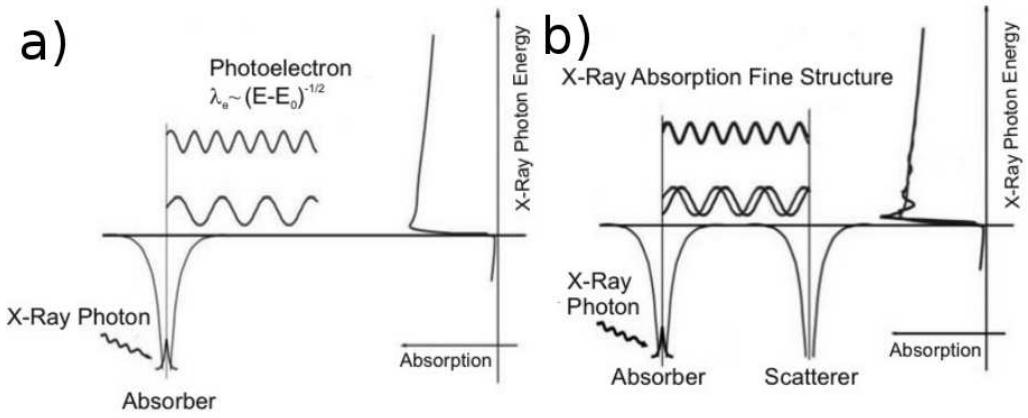


Figure 1.7: photoelectron wavefunction and absorption profile in the case of a single atom a) and in the case of two atoms, one creating and the second scattering the photoelectron b) Fine structure arising from the modification of the absorbing probability through the back-scattered photoelectron. Adapted from [49]

The techniques where this fine structure is revealed took the name of XAFS: X-ray Absorption Fine Structure. XANES, X-ray Absorption Near Edge Structure, involves the pre edge features and EXAFS, Extended X-ray Absorption Fine Structure, regards the post edge oscillating behaviour. There is no fundamental distinction in the physics involved in this two different regions [18], the differences came from the different energies involved: in XANES the transition occurs from a bound state to an unfilled-bound, quasi-bound or continuum-state, in EXAFS the transition take place only to continuum states. A photoelectron propagates in the material like a wave with a wavelegth $\lambda$ defined by De Broglie's law:

$$\lambda_e = \frac{2\pi}{k} = \frac{h}{m_e v} = \frac{h}{\sqrt{2m_e(h\nu - E_{bind})}} \tag{1.3.3}$$

In this equation it's clear that the wavelength of the electron is dependent from the energy of the incoming photon Fig. 1.8. In EXAFS, the wavelength of the electron is comparable with the inter atomic distance (a photon of an energy of $50eV$ bigger than the edge has a $\lambda \cong 1.72\mathring{A}$): the phenomenon can be explained as a single-scattering one. This means that this technique

can give information about the spatial arrangement of the atoms but not on the electronic structure. In the other hand XANES involves electron with bigger wavelength, coming from their smaller energies, this mean that multiple scattering processes are now allowed. This processes combined to the transition to bound and quasi-bound states make this technique capable of give information about chemical state and electronic structure.

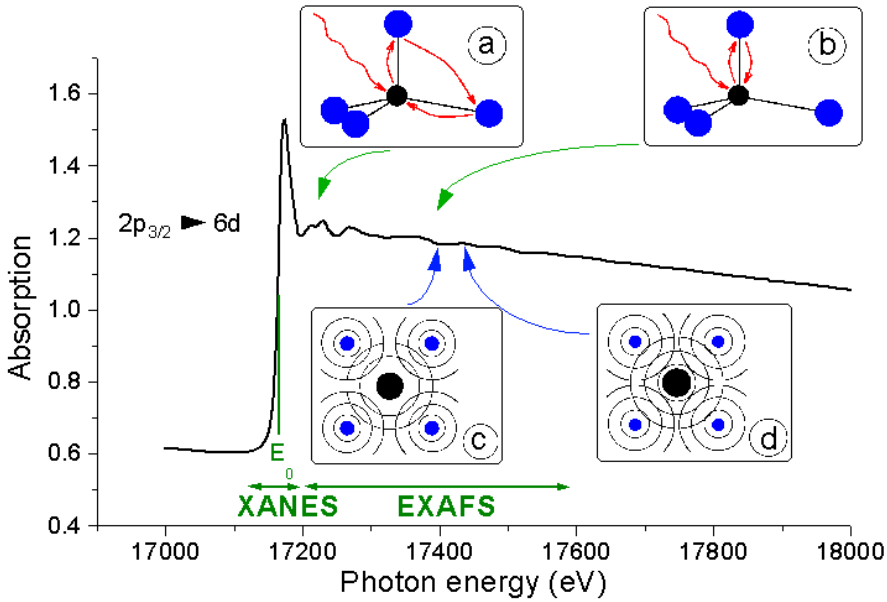


Figure 1.8: standard absorption spectra, on the spectrum are enlightened the XANES and EXAFS part and the phenomenon that take place in this region, [16]

### 1.3.1 EXAFS

The EXAFS region covers the high-energy continuum above the edge and it's characterized by an oscillating pattern in the spectra, which can be related to a single scattering event of an emitted electron with the surrounding atoms. In order to interpret the EXAFS oscillation $\chi(E)$, we consider the absorption well above the edge:

$$\chi(E) = \frac{\mu(E) - \mu_0(E)}{\Delta\mu_0(E)} \tag{1.3.4}$$

where $\mu_0(E)$ is the absorption spectrum of an isolated atom and $\Delta\mu_0(E)$ the normalization factor corresponding to the absorption edge jump (a step-like-

function that emulates the changing of absorption near the edge). At this point the total absorption coefficient $\mu(E)$ is the sum of the absorption of the isolated atom $\mu_0(E)$ plus a modulating function. Now an expression in the k space suits better for interferences explanation in electron scattering. Empirically eq. (1.3.5) explains this relation [8, 42, 49]

$$\chi(k) = \sum_i S_0^2 N_i \frac{|f_i(k)|}{kR_i^2} sin(2kR_i + \delta_c + \phi) e^{-2\sigma_i^2 k^2} e^{\frac{2R_i}{\lambda(k)}} \tag{1.3.5}$$

$|f_i(k)|$ and $\psi$ are amplitude complex electron scattering's modulus and phase, $\delta_c$ is the partial phase-shift due to the central absorbing atom, $S^2$ is a coherence loss constant reductive factor and N is the number of neighbour atoms at distance R. The summation must be taken over all groups of neighbour atoms because different atom kinds can be close to the central one. This groups are known as coordination shells. Each neighbour atom has a defined distance from the absorber and a well-defined scattering function depending also on Z. This makes EXAFS an **atom-species-sensitive** technique. The complete physical description requires more parameters: the exponential $e^{2\sigma_u^2 k^2}$ takes into account thermal disorder where $2\sigma_u^2$ is the Debye-Waller factor, the FWHM of the Gaussian distribution of interatomic distances in harmonic approximation, and $e^{\frac{2R_i}{\lambda(k)}}$ damps the signal as a consequence of the finite core-hole lifetime (recombination) and photoelectronic inelastic scattering, with the mean free path $\lambda(k)$. The dependence from $R^{-2}$ and $\lambda(k)$ explains the limit of about $5\mathring{A}$ to probe distance with this technique. The function $\chi(K)$ contains contributions of different frequencies coming from different inter-atomic distances: every coordination shell introduces a new frequency. Fourier based analysis is common in EXAFS [23], this allow one to extract structural information ($N$, $R$ and $\sigma 2$ ) from the spectra. Finally, it's important to underline the approximation under which eq. 1.3.5 is derived: the potential energy in the solid is approximated as constant between spherically symmetric atoms (the muffin-tin approximation), only an electron could be excited and it interacts with the electron gas in the solid. Only back-scattering (elastic) from neighbouring atom is included and multiple

scattering is neglected, as explained before has low importance in this case than in XANES. Nevertheless there are approaches that take into account multiple scattering processes in the EXAFS analysis [54, 53]

### 1.3.2 XANES

The XANES part of the XAS spectrum is usually 10-50 eV above the edge. In this region the signal is usually much stronger than the EXAFS oscillation. This opens to the possibility to perform successful experiments on more diluted sample. On the other hand the single scattering approximation doesn't hold anymore and this leads to more complicate models for the interpretation of the XANES region: solving Fermi's golden rule integrals with a full Hamiltonian is in principle possible, but lacking of initial and final electronic wavefunction for real systems complicates the task a lot. For this reason, approximations must be made and implemented in numerical calculations. If reasonable approximations are taken into account XANES reveals both structural and electronic information. The first absorption features appears when energy exceeds the Fermi level by 5-10 eV and the pre-edge region has a physical origin which is different for each class of materials: bound valence states, core exciton in ionic crystals, unoccupied local electronic states in metals and insulators, etc. Above the Fermi energy and just below the ionization threshold there is the white line: the strong absorption peak. The name comes from past experiments when white peaks appeared in detector film plates in this spectral region. The physical origin of such a peak is the transition to empty states spatially localized close to the atom giving a high overlap between initial and final state wave functions. Finally, the region after the white line is governed by multiple scattering events determined by the geometrical arrangement of the atoms in the local cluster around the absorber. XANES can be described qualitatively in terms of:

1. neighbour atom coordination chemistry

2. molecular orbital structure (crystal field splitting, d-d interaction, p-d

hybridization etc.)

3. band structure

4. photoelectron's multiple scattering

The appearing and the shape of forbidden transition gives information about the geometry of the surrounding atoms. This complex physics at the origin of the spectral shape in the XANES region calls for a strong theoretical approach to the problem, fortunately the power of modern calculus helps us to interpret this kind of data. The methods used to calculate the ground and final state wave functions as well as the photo-induced electronic transitions are various. Each of them has its strengths to describe certain aspects and properties of the XANES spectrum, but this will not be treated in this thesis [51].

## 1.4 Conclusion

This first chapter covers the basis of X-ray matter interaction with a description of the two techniques that will be used in this work EXAFS and XANES. The first one involves the post edge region and gives mostly structure information with a relatively easy analysis, the second one covers the region around the edge and provides both, structural and electronical information with a more complicated analysis.

# Chapter 2

# Experimental techniques

This chapter describes the basic principles that govern the functioning of a synchrotron, from the physics of the radiation emission to more technical and engineering aspects. The second part describes the beam line ID24 at the ESRF and the experimental set-up for cryogenic temperature pulsed magnetic field absorption experiments.

## 2.1 Synchrotron radiation

The Synchrotron is a facility where electron are accelerated to create highly collimated X-rays. This kind of electromagnetic radiation is called synchrotron radiation (SR). The first observation of synchrotron radiation took place in 1947 in the General Electric Research Laboratory - New York. In a few years the scientific community realized that this was the most intense and versatile source of X-rays for scientific purpose discovered until then. For this reason storage rings stopped to be dedicated just to high energy nuclear physics experiments and started to be used for the first generation synchrotron facilities: the first spectrum was measured in Tantalus I in 1968. The design and operating conditions of these facilities were not optimized for X-ray experiments and this was the main limiting factor of the output of synchrotron radiation. The first facility, designed as a dedicated synchrotron radiation source started operation in 1981 and was called the 2GeV SRS,

Synchrotron Radiation Source, in the UK. It was followed by the construction of many other synchrotrons, like NSLS, BESSY or LURE. This history has culminated in the 3rd generation synchrotron sources like ESRF - European Synchrotron Radiation Facility 1012 times brighter than the early lab based sources, Fig. 2.2.


Figure 2.1: Picture of the European Syncrotron Radiation Facility [5]

### 2.1.1 Radiation emission of accelerated charges

The emission of radiation from accelerated charges was already known before the theory of relativity and quantum mechanics. The power emitted from a Larmor oscillating dipole can be derived from Maxwell's equations:

$$P = \frac{e^2 \vec{a}^2}{6\pi\epsilon_0 c^3} \tag{2.1.1}$$

Eq. 2.1.1 is valid for a non-relativistic electron motion which radiates isotropically in space, but in the case of synchrotron, the electrons travel nearly at the speed of light. A relativistic generalization has been derived using the Lienard-Wiechert fields, relativistic solution of Maxwell equations with Q and J as a single charged moving particle, and calculating the flux of the Poynting vector to derive the emitting power [36]:

$$P = \frac{e^2}{6\pi\epsilon_0 c^3}\gamma^6 \left[ \dot{\vec{v}}^2 - \frac{(\vec{v} \times \dot{\vec{v}})^2}{c^2} \right] \tag{2.1.2}$$

with $\gamma = \frac{1}{\sqrt{1-\beta^2}} = \frac{E_0}{m_e c^2}$ that is its energy in rest units. Eq. 2.1.2 doesn't have an angular term because it is integrated over the solid angle. In synchrotrons, bending magnets apply magnetic fields forcing the particles to turn. For a relativistic particle with high energy, moving on circular orbit of radius R the emitting power becomes:

$$P = \frac{e^4}{6\pi\epsilon_0 c^5 m_0^4}\gamma^4 |\dot{\vec{v}}|^2 \tag{2.1.3}$$

The field of a bending magnet is oriented perpendicular to the motion of the electron and the radius of curvature R can be derived from setting the Lorenz force equal to the centripetal force:

$$R = \frac{m_0^2 c^3 \gamma^2}{eEB} \tag{2.1.4}$$

and then

$$P = \frac{e^4}{6\pi\epsilon_0 c^5 m_0^4} E^2 B^2 \tag{2.1.5}$$

In this equation it is clear, that the forth power dependence on the mass allows only really light particle like positrons or electrons to be used in a synchrotron: the equation is strongly dependent on $B^2$ and $1/R^2$. From this equations it is possible to calculate the amount of power dissipated on a round trip in the ring:

$$\Delta E = \frac{2\pi R}{v} P = \frac{e^2 v^3 \gamma 4}{3\epsilon_0 c^3 R} \tag{2.1.6}$$

for electrons in a synchrotron $v \sim c$ and the expressure can be rewritten as:

$$\Delta E(Mev) = 8.85 \cdot 10^{-2} \frac{[E(GeV)]^4}{R(m)} \tag{2.1.7}$$

this means that the particles lose energy really fast and it has to be restored in some way. In synchrotron this is done via Radio-Frequency oscillating electric fields.

### 2.1.2 Synchrotron structure

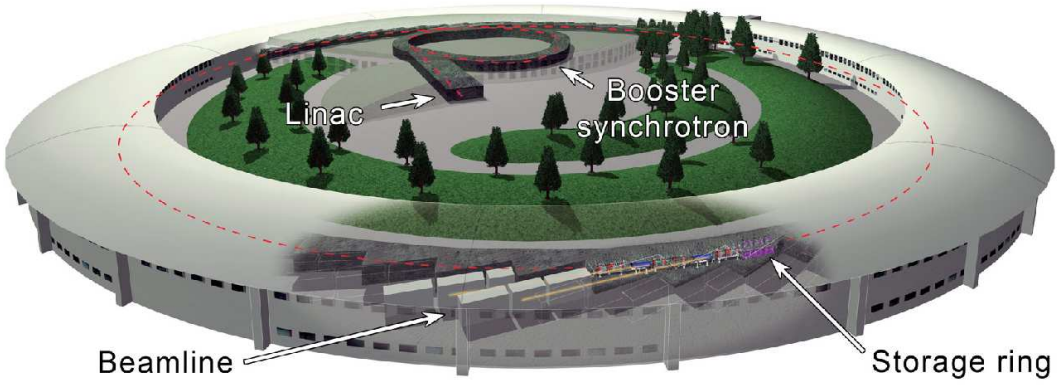


Figure 2.2: Typical scheme of a storage ring [2]

Fig. 2.2 shows a typical third generation synchrotron facility. Electrons are produced by an electron gun and accelerated by the Linac - Linear Accelerator inside the storage ring, it rises their energy to $200MeV$ before they enter in the booster ring. Here they are accelerated up to $6GeV$ with cavities. Now they can be injected in the storage ring doing 350000 rounds per second (for ESRF) for many hours, to achieve this results they must stay in UHV - Ultra High Vacuum level: $10^{-9}$- $10^{-11}mbar$. At ESRF the average lifetime of an electron in the storage ring is $100h$ (in multibunch mode), during this time it emits SR for all the beam line, this lifetime is due to scattering events or recombination causing its loosing. The energy loss of the electrons in the ring is restored by cavities. To summarize, a modern synchrotron is composed by:

1. Injection system, composed by Linac and booster ring.
2. The UHV system to keep the pressure in range
3. The RF - Radio Frequency system this is a radio frequency ($352.2MHz$ at the ESRF) electric field used to supply energy to electrons in the storage ring after radiation loss.
4. The supplying time is called "refill", in this periods all the electron inside the beam are replaced by new one re-injected. The storage ring

is never uniformly filled by electrons, but they are grouped in packages called bunches containing a variable number of them. The number of bucket in a synchrotron is defined by the radio frequency and the geometry of the ring, Fig. 2.3. Due to the RF voltage and phase stability conditions each bucket in the accelerator is equally distributed around the machine and the length between two bunches is therefore equal to the Radio Frequency wavelength. Then, the maximum number of bunches present in the ring is given by the ratio between the ring length and the RF wavelength.

5. A set of Magnet guarantee the electron poligonal orbit in the storage ring

In the next section, the magnet and the RF system will be described.

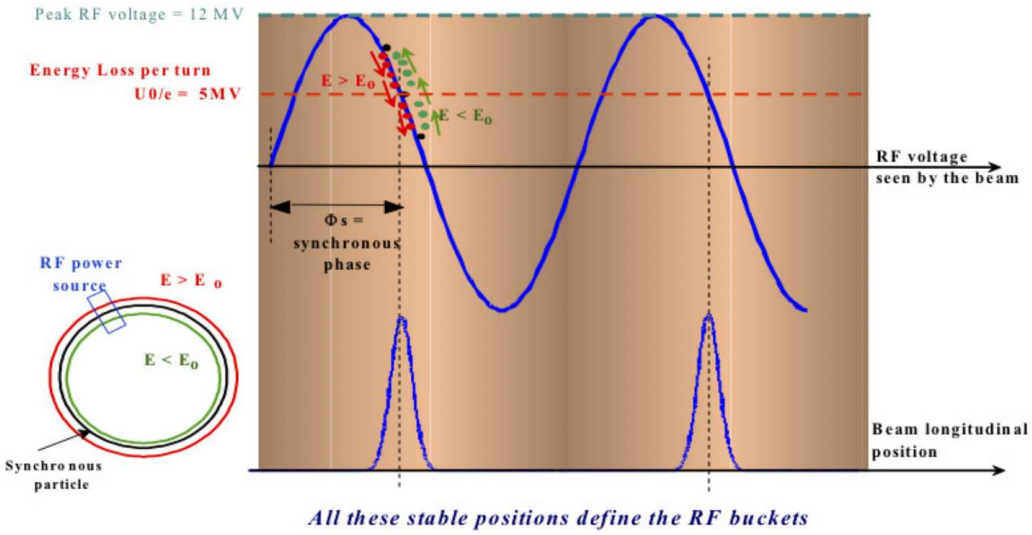


Figure 2.3: Radio Frequency field used to restore energy to the electrons. The lowest part shows how electrons are placed in a certain position in space [2].

### 2.1.3 Magnets

Different types of magnets confine the electrons on a circular orbit and generate synchrotron radiation inside the storage ring:

1. **Bending magnet** also called dipole magnet. They are the simplest and are used mostly to curve the orbit, in fact the storage ring is not a perfect circle but is composed by straight sections separated by dipole magnets. Inside these magnets the electrons emit radiation in the plane of the storage ring, Fig 2.4.

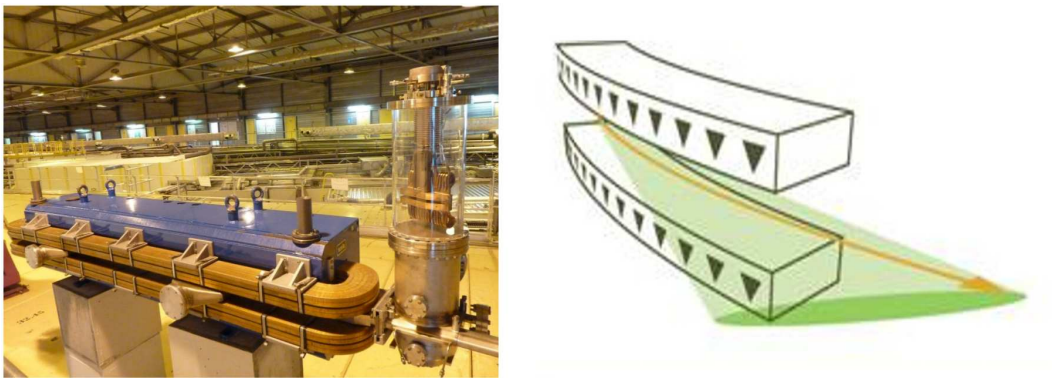

Figure 2.4: left: ESRF bending magnet. Right: schematic picture of bending magnet emission [1].

X-rays emitted from a bending magnet appear to be in the plane of the circular orbit for an observer near the storage ring . This collimation is the results of the speed of electrons: near the speed of light all the emitted radiation is confined in a small cone defined by an angle of:

$$\theta \sim \frac{1}{\gamma} \tag{2.1.8}$$

this angle is called natural opening angle; this is typically of the order of 0.1-1$mrad$ [13, 36]

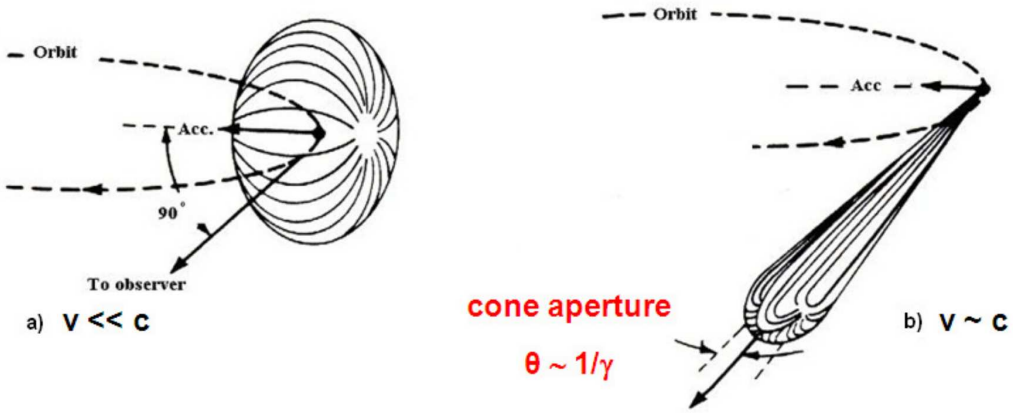


Figure 2.5: comparison between the radiation emission of a non relativistic and relativistic charged particle. This picture explains the high collimated radiation emission of synchrotron [30].

The emission frequency of the magnet can be estimated using a general derivation based on the length of a radiation pulse seen by an observer. This can be seen as the difference in travel time $\Delta t$ between the electron and the radiation just emitted, travelling from $A$ to $A'$, Fig. 2.6.

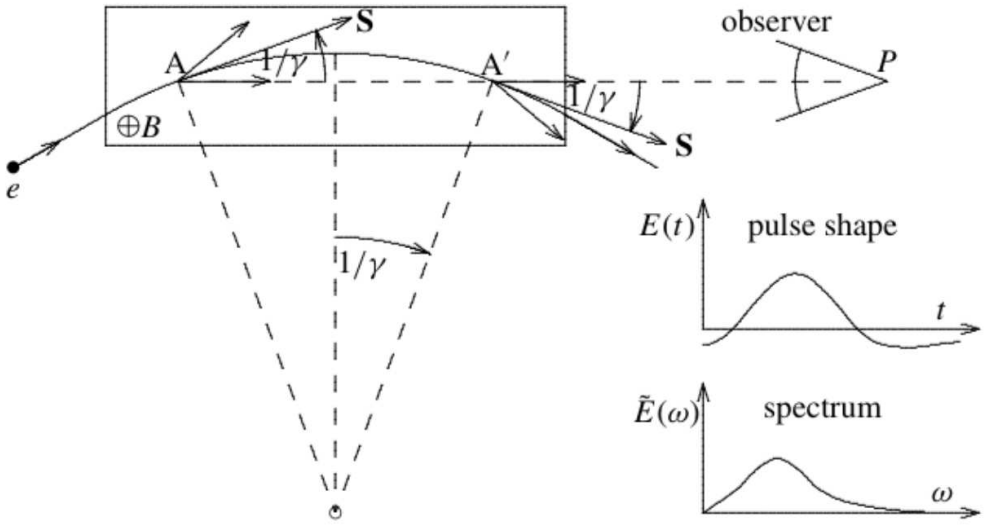


Figure 2.6: path of electrons in a bending magnet, the observer sees the radiation emitted between $A$ and $A'$ [36]

$$\Delta t = t_{el} - t_{ph} = \frac{AA'}{v} - \frac{AA'}{c} = \frac{2R\theta}{\beta c} - \frac{2R\sin\theta}{c} = \frac{2R}{c}\left(\frac{1}{\beta\gamma} - \sin\left(\frac{1}{\gamma}\right)\right) \tag{2.1.9}$$

it was used the approximation on $\theta \sim \frac{1}{\gamma}$. For relativistic electrons the sin function can be linearly expanded:

$$\Delta t \sim \frac{2R}{c\gamma\beta}\left(1 - \beta + \frac{\beta}{6\gamma^2}\right) \sim \frac{2R}{c\gamma\beta}\left(\frac{1}{\gamma^2} + \frac{\beta}{3\gamma^2}\right) \sim \frac{4R}{3c\gamma^3} \tag{2.1.10}$$

where $1 - \beta \sim \frac{1}{2\gamma^2}$. Thanks to the Heisenberg relation we obtain the typical frequency of the spectrum $\gamma$:

$$\gamma \sim \frac{3c\gamma^3}{4R} \tag{2.1.11}$$

A quantitative derivation is possible involving Bessel function dependences [13, 36]. The resulting spectrum is very broad and continuous over an extended wavelength range, limited by the so called *critical photon energy* $E_c$:

$$E_c = \hbar\omega_c = \frac{3e\hbar B\gamma^2}{2m_0} \tag{2.1.12}$$

where $B$ is the magnetic field. This is the energy which divides the spectrum of the emitted photons in a half. Half of them have higher, and half lower energy.

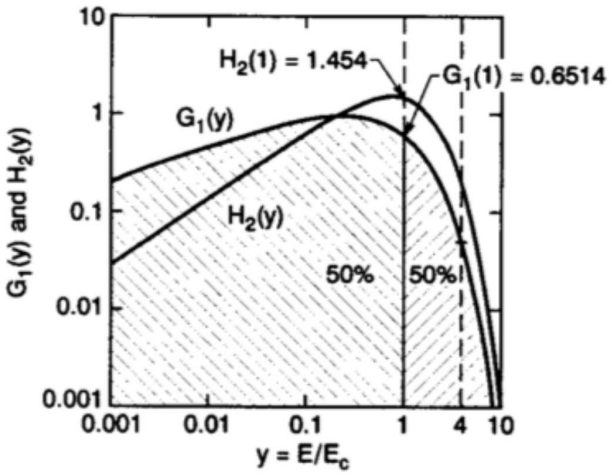


Figure 2.7: $H_2(y)$ is the bending magnet on-axis and $G_1(y)$ is the vertically integrated photon flux [36].

The relation between *critical photon energy* and magnetic field strongly involves the ring geometry. $B$ inside the magnet is difficult once fixed to be changed and than the emitted power and *critical photon energy* are fixed in project phase.

The radiation emitted by a bending magnet is linearly polarized in the ring plane and elliptically polarized outside that plane [65].

2. Additional **quadrupole and sextupole magnets**, Fig. 2.8 are placed in the straight section of the ring. Their function is to focus the elctron beam and to maintain the ideal circular orbit and correct the beam energy aberration.

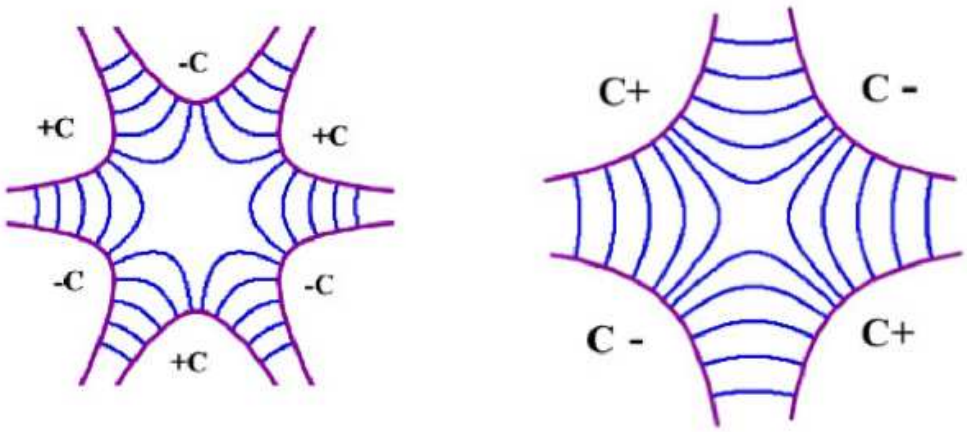


Figure 2.8: left sxtupole magnet, right quadrupole magnet [30]

3. **Insertion devices** are periodic magnetic structures inserted into the straight section of the ring that generate brilliant, directional an monochromatic SR. There are two different type of ID: **wigglers** and **undulators** which are similar in structure but provide a different type of SR, Fig. 2.9.

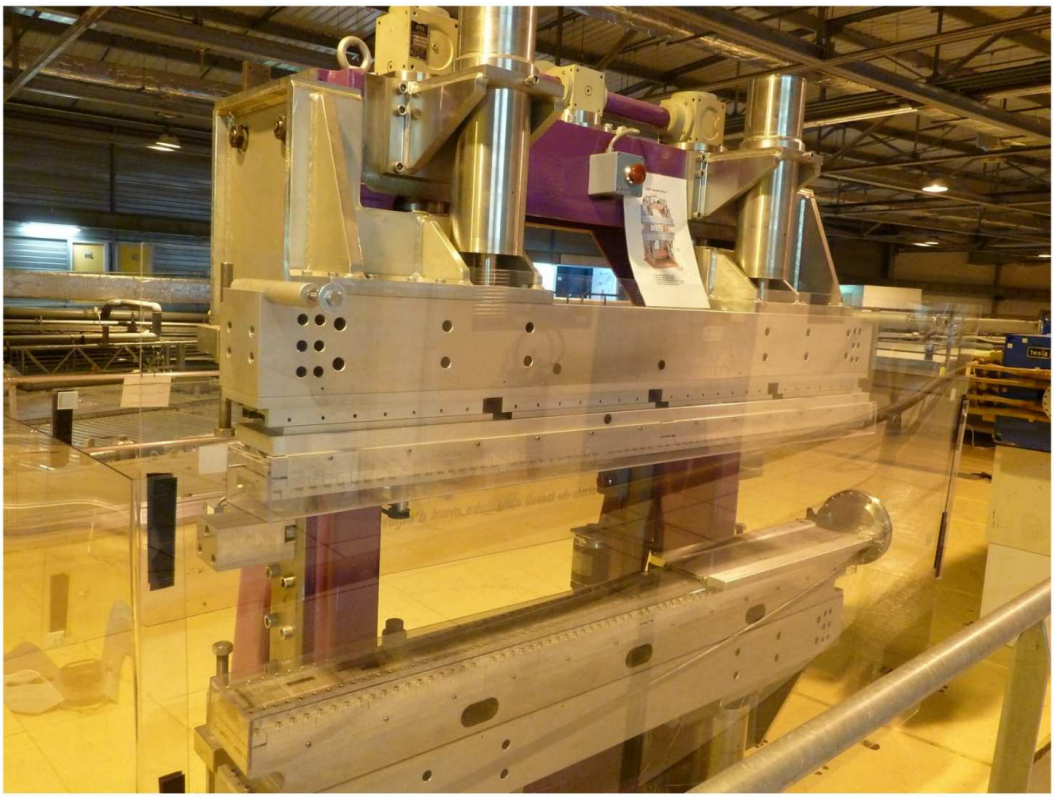

Figure 2.9: insertion device (undulator) at ESRF.

They consist of a periodic magnet structure with vertical alternating magnetic fields with length $L = N\lambda_u$ where N is the number of magnetic poles and $\gamma_u$ is their period. The fields varies sinusoidally along the undulator axis. Travelling electrons will experiment a sinusoidal motion in horizontal plane due to the variable $B$, this kind of motion can be described with the deflection parameter $K$ [13, 43] given by:

$$K = \frac{eB\gamma_u}{2\pi m_0 c} = 0.9337 \times \lambda_u[cm] \times B[T] \tag{2.1.13}$$

The maximum angular deflection of the electrons equals to $\delta = \frac{k}{\gamma}$, this parameter distinguishes *undulators* from *wigglers*, Fig. 2.10. For the former $K \leq 1$ and the radiation from adjacent periods will interfere coherently. This happens because the angular deflection of the electrons lies in the $\frac{1}{\lambda}$ radiation cone. The spectrum is then composed by sharp peaks at the harmonics of the fundamental wavelength and can be

derived by the undulator equation:

$$E_n[keV] = 0.9496 \times \frac{nE_e^2[GeV]}{\lambda_u[cm] \times \left(1 + \frac{K^2}{2} + \gamma^2\theta^2\right)} \tag{2.1.14}$$

This means that the energy of the fundamental radiation and its harmonic can be tuned by the strength of the magnetic field, this can be done by adjusting the gap between the magnetic structures. This provides a fully tunable X-ray source; even harmonics radiate off-axis but their contribution is really low compared to the odd one. The relative bandwidth of the $N^{th}$ harmonic can be expressed as:

$$\frac{\Delta\lambda}{\lambda} = \frac{\Delta\omega}{\omega} = \frac{1}{nN}(N = 1, 2, 3...) \tag{2.1.15}$$

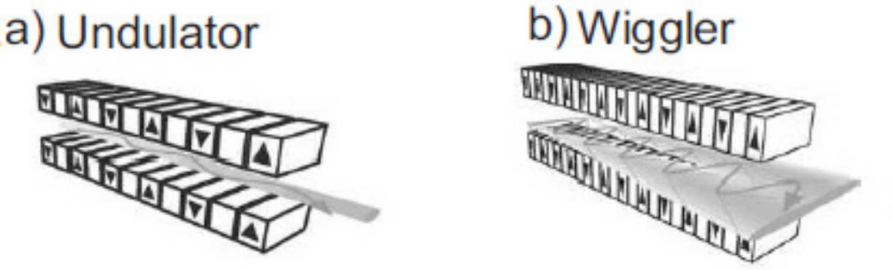


Figure 2.10: a) undulator and b) wiggler [32]

With a strong magnetic field, and thus $K \gg 1$, coherence effects become really small for the high angular separation of radiation originating from different segments and after a short distance they simply don't overlap anymore. In this situation relativistic effects cause a distortion of the motion that generates many harmonics of the single undulator wavelength. The radiation from different parts of the electron trajectory adds up incoherently and the resulting spectrum merges all produced harmonics into a broad and continuous distribution similar to a bend magnet spectrum. The difference lies in the intensity of

the emitted radiation, in the wiggler case it is 2N times more compared to bending magnet, Fig. 2.11. .

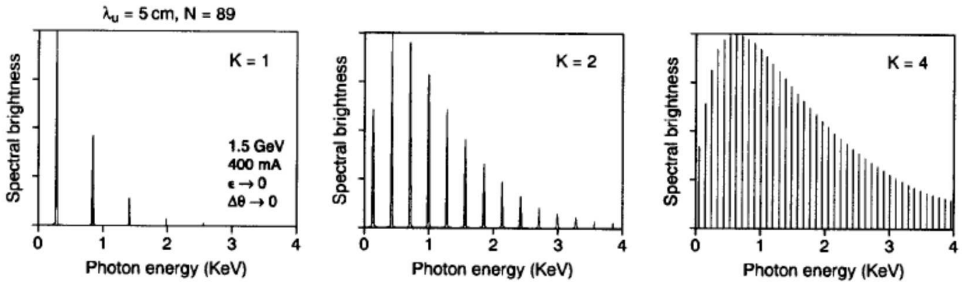


Figure 2.11: undulator radiation as a function of the $K$ parameter. The wiggler spectrum can collapse into continuum spectrum as consequence of non-ideal effects like finite emittance or a big acceptance angle [13]

The total power irradiated by an undulator or wiggler is:

$$P_T = \frac{N}{6} Z_0 I e \frac{2\pi c}{\lambda_u} \gamma^2 K^2 \tag{2.1.16}$$

where $Z_0 = 377\Omega$ or

$$P_T[KW] = 0.633 \times E^2 B^2 L I[GeV^2 T^2 mA] \tag{2.1.17}$$

Due to the deflection of the e-beam in a plane the produced radiation is linearly polarized. To achieve a circular polarization the insertion device can be modified to produce a spiral motion of the electron [65]. This kind of polarized light is useful to study polarization dependent material properties, such magnetism.

## 2.2 Experimental Set-up

### 2.2.1 Beamline description

All this work took place at ID24 and BM23 at the ESRF, as the name suggests, the X-ray source in ID24 is an insertion device in a straight section

of the ring. The beam line placement inside the synchrotron alternates an ID with a BM, the second one is clearly based on a bending magnet as a source of X-rays. As explained before the X-ray flux at ID beam lines is much higher than at BMs. At ID24 it is possible to obtain a flux up to $2 \cdot 10^{14} ph/s$. This high flux in combination with the energy dispersive beam line design allow one to perform time resolved spectroscopy of the sample under study, Fig 2.12.

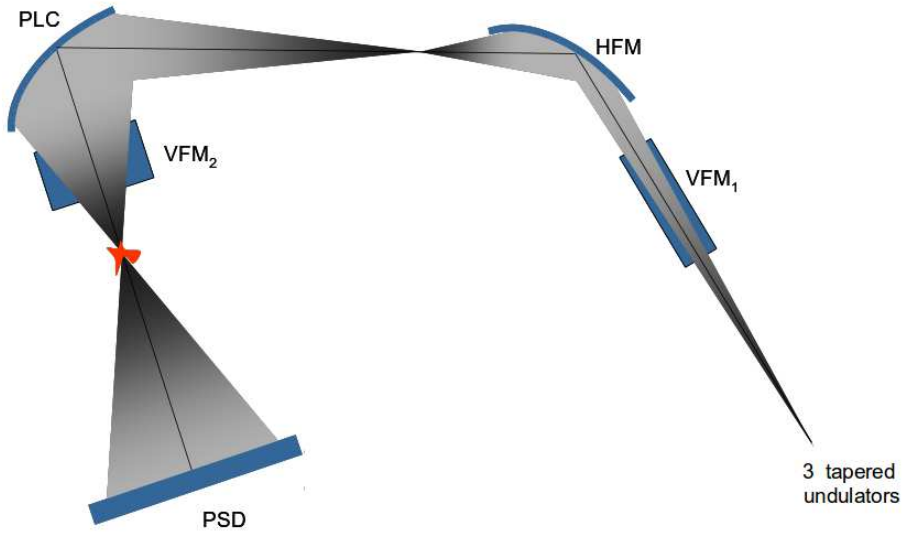


Figure 2.12: simple scheme of ID24, the incoming X-rays from 3 undulators are focussed vertically by VFM1 - Vertical Focussing Mirror 1. After that, the HFM - Horizontal Focussing Mirror creates a flux divergence to illuminate the PLC - Polychromator, to refocus all the energies horizontally in the focal spot, VFM2 - Vertical Focussing Mirror 2 and the PSD: a CCD detector [50].

The main feature of this beam line is the possibility to acquire a full energy spectrum in one CCD image, the acquisition time for an Iron spectrum is around $2\mu s$ with a focal spot of $5 \times 5\mu m$. Let's analyse more in detail the principle of the energy dispersive design Fig. 2.13. The design is based on an elliptical geometry, the X-ray source is place in one focal spot of the ellipse, and the sample under study is placed in the other one.

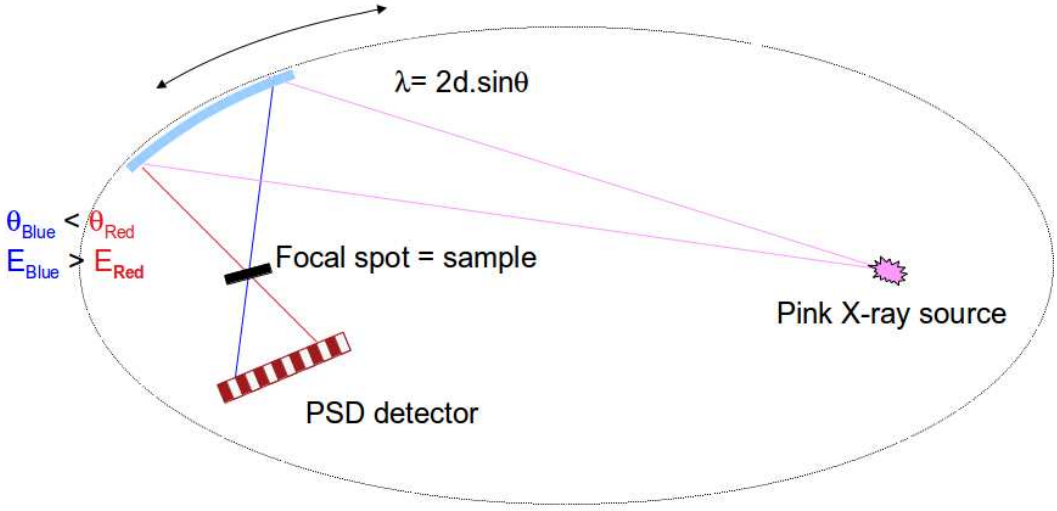


Figure 2.13: raffiguration of the elliptical shape of the polychromatic. The pink source is placed in a focus of the ellipse and diverges the X-rays flux, the polychromatic than provide to energy selection and focalization in the focal spot. [50].

The bisectional property of the ellipse assure that a ray emitted from one focus, reflected from the surface of the ellipse always converge on the second focus. In ID24 the reflection of the X-rays on the ellipse surface is provided by a foil of silicon with the 111 face exposed to X-ray called **polychromator**. The reflection on the 111 surface is obtained by fulfilling the Bragg condition for the incoming X-ray, the position of incidence on the polychromator is than related with the energy of the X-ray reflected for the changing of the incident angle due to the bending of the silicon crystal to follow the elliptical shape. The reflected beam is dispersed in energy and converge on the sample, the acquisition of the beam is made with a positional sensitive detector, in ID24 case is a CCD. The pixel position of the sensor is than related with a certain energy. This ID24 design allow the acquisition of a full energy spectrum in one CCD shot.

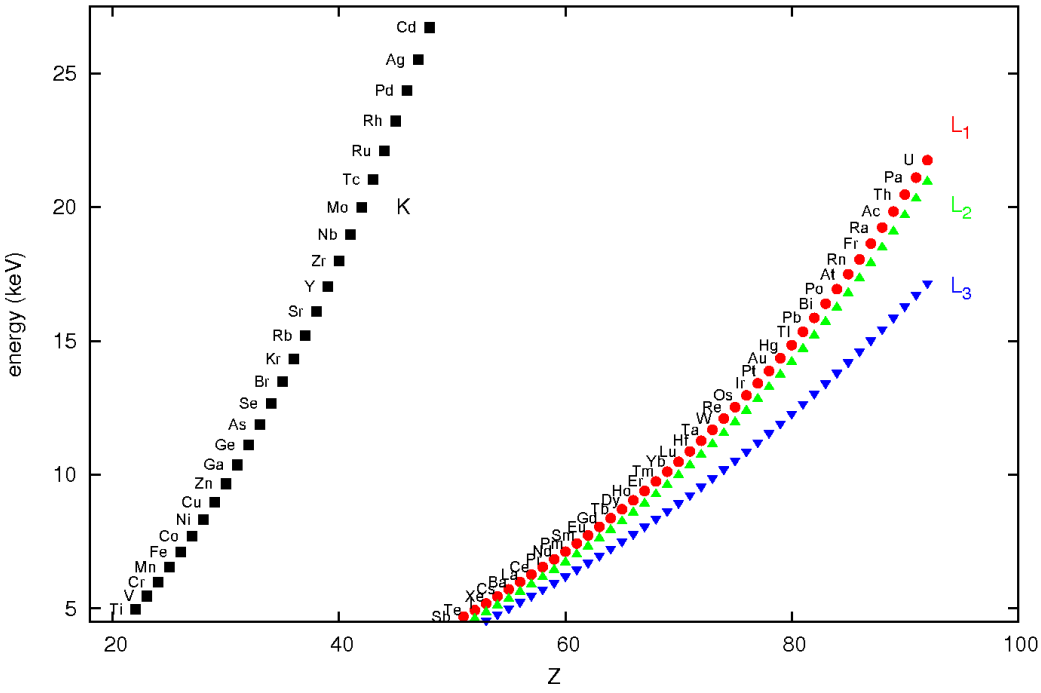


Figure 2.14: absorption edges accessible at ID24. [courtesy of Cornelius Strohm]

For selecting the energy for spectrum acquisition is necessary to have the possibility to move all the experimental set-up over the angle determined by the Bragg condition of the polychromator, Fig. 2.15. The direction of the incoming beam before the polychromator is fixed, than to analyse different energies the experimental set-up has to be moved along the angle that corresponds to the reflected beam by the polychromator. From this geometry comes the $\theta - 2\theta$ relation, a variation in angle between the beam an the polychromator corresponds to a double variation of the angle of the reflected beam respect the incoming one.

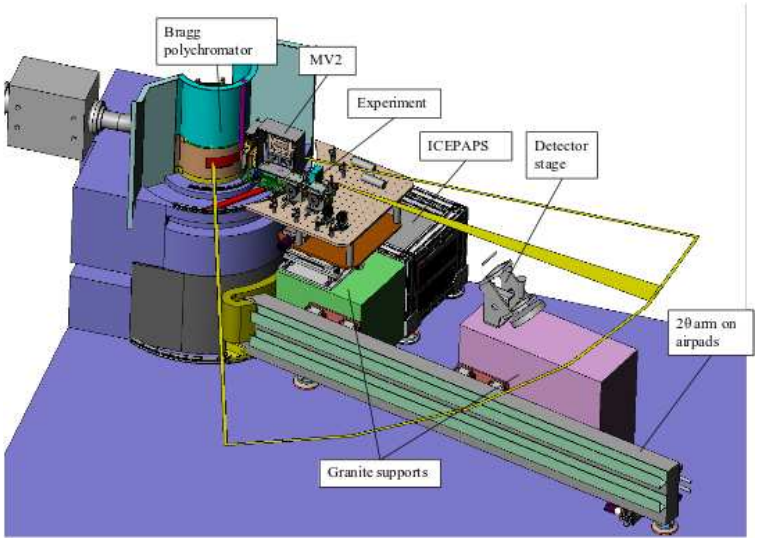


Figure 2.15: design of one of the hutches of ID24. The image shows the angular range over where the experimental set-up can be moved. [courtesy of Trevor Mairs]

### 2.2.2 Experimental set-up

Fig. 2.16 shows the experimental set-up for experiment in multi-extreme conditions in the L hutch of ID24.

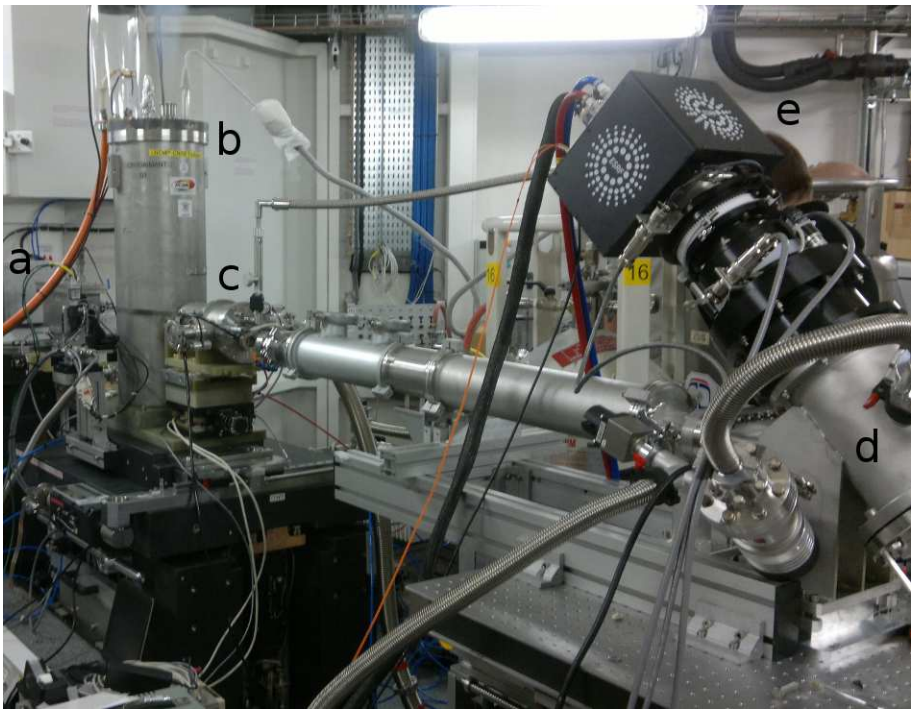


Figure 2.16: picture of the experimental set-up inside the L hutch of ID24. **a** VFM2 - Vertical Focussing Mirror 2, **b** $Cu$ coil in liquid Nitrogen for pulsed field, **c** He flow cryostat, **d** fluorescence screen, and **e** CCD for acquisition.

1. **Magnet**: the pulsed magnet is provided by the LNCMP - Laboratoire National des Champs Magnétiques Pulsés, Toulouse. It's a $Cu$ coil immersed in liquid Nitrogen linked to a set of capacitors that provide the necessary charge for field production. The basic principle is a simple LC circuit that discharge in resonance. The pulse shape and circuit with a charge and discharge sequence is shown in Fig. 2.17.

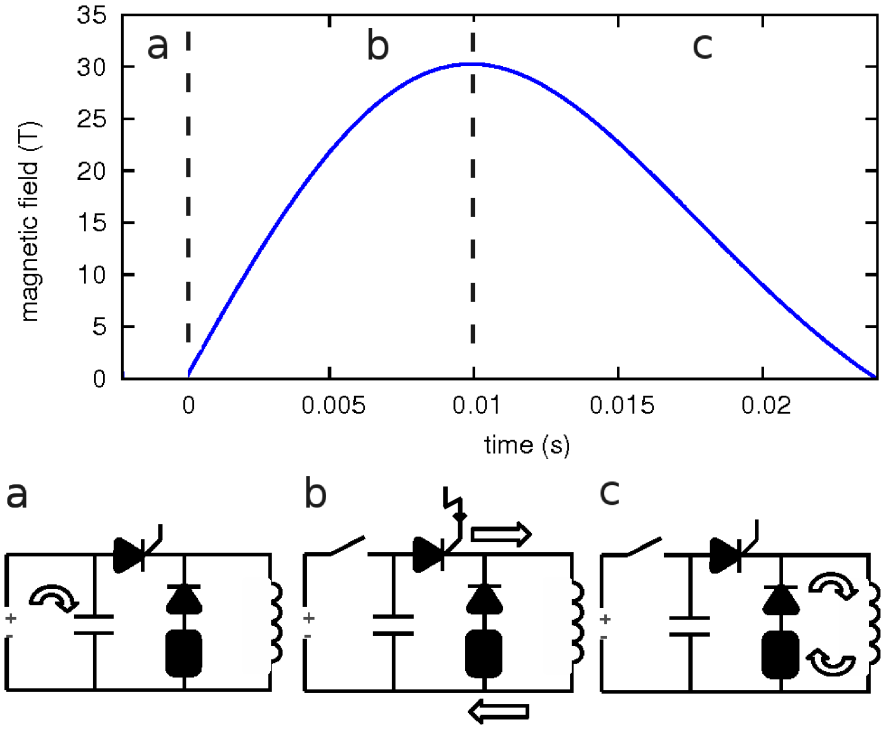


Figure 2.17: Charge, discharge sequence of the magnet circuit. a) charge before the pulse, the thyristor is closed. b) Deconnection of the charger and firing opening of the thyristor, the current can flow from the capacitor to the coil. c) removing of the triggering voltage on the thyristor to avoid the resonance of the LC circuit and the oscillation of the magnetic field, the current in the circuits flow through the coil and diodes up to the end of the pulse.

In Fig. 2.18 shows a 3D model of the magnet with the cryostat.

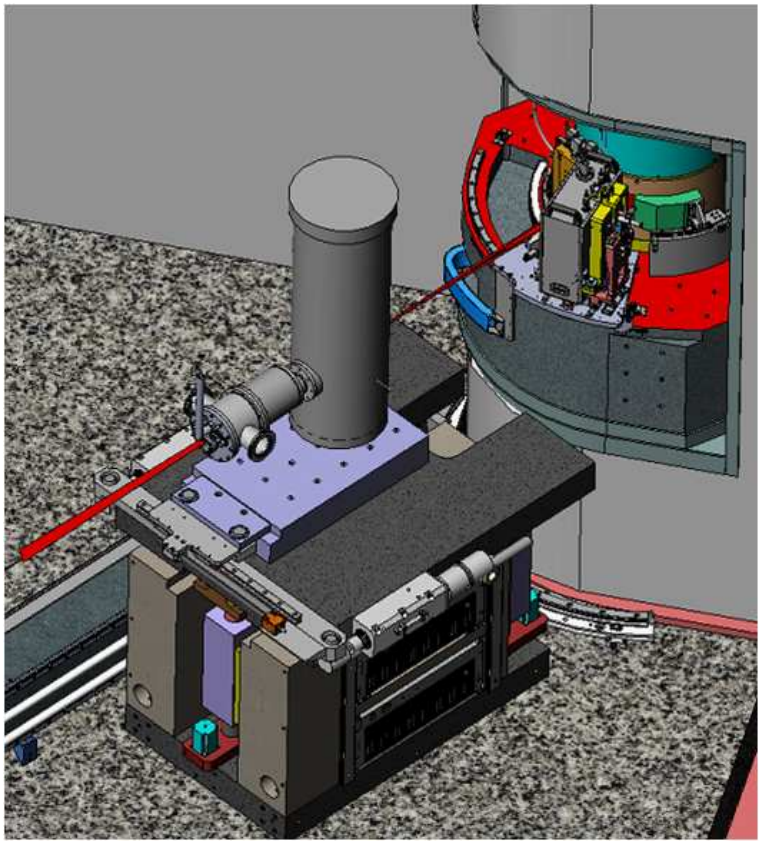

Figure 2.18: drawing of the magnet mounted with the cryostat, the red line materializes the direction of the X-rays. [courtesy of Trevor Mairs].

2. **Cryostat**: the He-flow cryostat, Fig. 3.1, is designed to fit into the magnet, the Helium flows between two concentric tubes (green), cools the sample or the cell (mounted at the end of the green tube witch is in the centre of the coil) and is recovered along the beam path. The recovering near the flowing channel of the Helium helps the cooling down of the gas. This cryostat can operate from ambient temperature to $1.5K$.

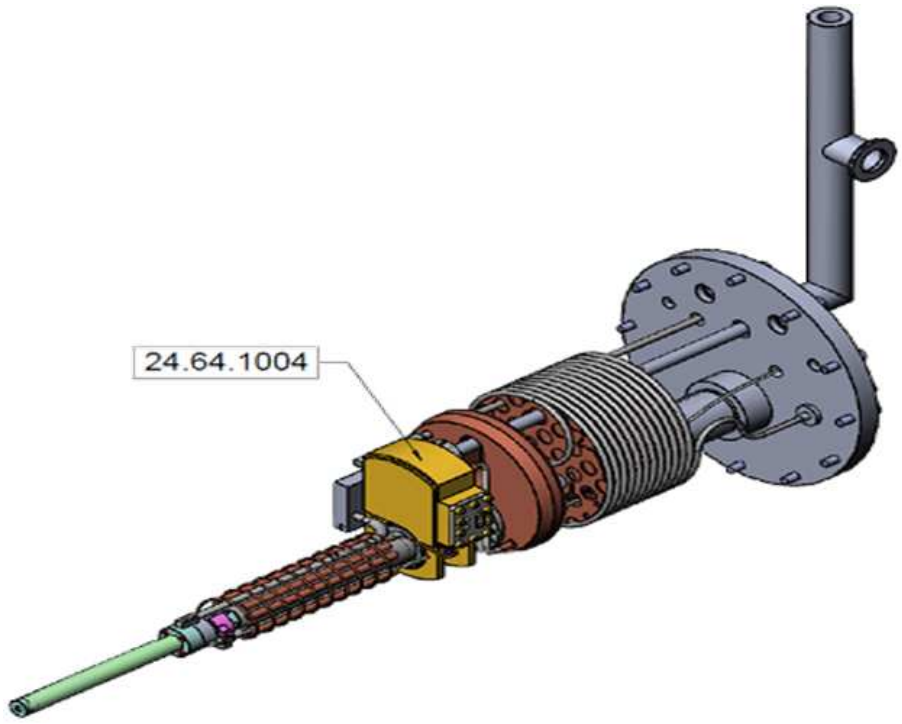


Figure 2.19: drawing of the cryostat, [courtesy of Peter Van Der Linden]

## 2.3 Conclusion

Synchrotron radiation is a powerful tool to investigate matter and electronic structure. The acceleration of electrons in a storage produce X-rays to be used in beam lines, this is made with 3 different methods *bending magnet*, *undulators* and *wigglers*. These three methods were described in this section. Furthermore the beam line ID24 was introduced. The simultaneous acquisition scheme of the energy dispersive technique makes this beam line particularly suited for time resolved experiments as for example in pulsed magnetic fields. After we described the experimental set-up with the pulsed magnet and the cryostat.

# Chapter 3

# Strongly correlated electron systems

**Strongly correlated electron systems** are a wide class of materials with strange electronic and magnetic properties: the main feature that characterizes these materials is the impossibility to describe their electronic properties with a non-interactive electron model. The approximation of single particle electrons that leads to the metallic sea in the Drude theory can't describe the features of these systems. At this kind material belongs many transition oxides, this are usually characterized by an unfilled $d$- or $f$- electron shell with narrow band. As said before electrons' interaction can't be simply expressed with the Drude's mean field theory, electrons has a complex interaction between themselves. This leads to various classes of materials deeply studied in this year: spintronic materials, heavy fermion, high-T superconductivity in cuprates and others. The argument of this chapter regards **heavy fermion** and I will analyse their physics in more in detail.

## 3.1 Heavy fermion

The term **heavy fermion** describe the electronic excitations in a new class of inter-metallic compound with an electronic density of states 1000 lager than Copper, this class include superconductors, antiferromagnet and insulators

[59]. The goal of modern condensed matter research is to couple magnetic and electronic properties to develop new classes of materials with high technological interest, such as ambient temperature superconductors, colossal magnetoresistance- or spintronic-materials. In this material magnetic and electronic properties couple together in different and not-yet well understood ways. Many of these materials contain rare earth or actinide ions forming a matrix of localized magnetic moments. The interaction of these moments with a sea of conduction electrons is at the origin of the particular physics of these compounds. In most rare earth metals and insulators, local moments tend to order antiferromagnetically, but in heavy fermions the quantum mechanical local moment vibration induced by delocalized electrons is strong enough to melt magnetic order. The mechanism involved in this reshuffling is called Kondo effect [40, 41]: this effect expects that a free magnetic ion, with a Curie magnetic susceptibility ad high T, becomes screened by the spins of the conduction sea to form a spinless scattering centre at low temperature and low magnetic field.

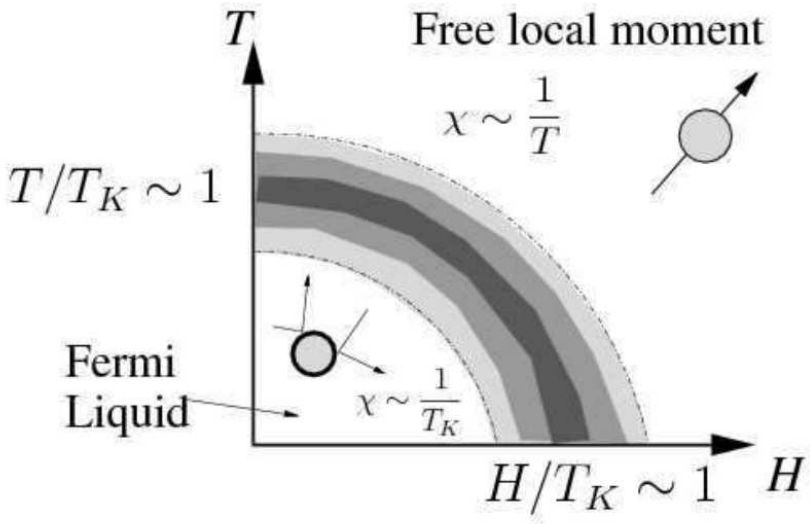


Figure 3.1: In the Kondo effect, local moments are free at high temperatures and high fields, but become screened at temperatures and magnetic fields that are small compared with the Kondo temperature $T_K$ forming resonant scattering centres for the electron fluid. The magnetic susceptibility $\chi$ changes from a Curie law $\chi \sim \frac{1}{T}$ at high temperature to a constant paramagnetic value $\chi \sim \frac{1}{T_K}$ low temperatures and fields. [58]

The effect takes place when the temperature or magnetic field drops below $T_K$, Kondo temperature, than this ions act as strong scattering centres for electrons witch explains the high resistivity produced by isolated magnetic ions. When this effect take place in a lattice the quenching is present in each material site, this leads to coherence of the scattering witch involves a resistivity drop at low temperature. In lattice the effect may also be visualized as a dissolution of localized $f$ electrons into the quantum conduction sea [24]. They then became electrons with radically enhanced mass, the net effect of this process results in an increase in volume of the electronic Fermi surface and a transformation of electronic mass and interaction. Fig. 3.2

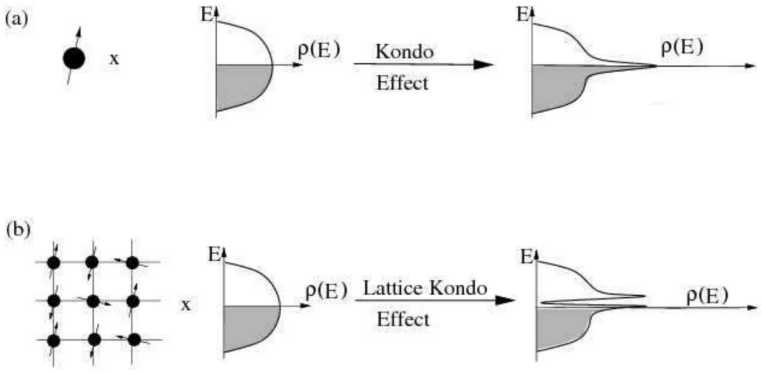


Figure 3.2: **a** single impurity Kondo effect creates a single fermionic level into the conduction sea witch leads to a resonance in the conduction electron density of states. **b** Lattice Kondo effect builds a fermionic resonance into the conduction sea in each unit cell witch leads to the creation of an heavy electron band of width $T_K$

It's clear from this picture, that the energy position of the Fermi level decides which kind of material we are observing. If it falls in the gap of the electronic band we are facing a **Kondo insulator**

### 3.1.1 Kondo Insulator

The ability of a dense lattice of local moments to transform a metal to an insulator is one of the most visible consequences of the **dense Kondo effect** [10, 55, 64].

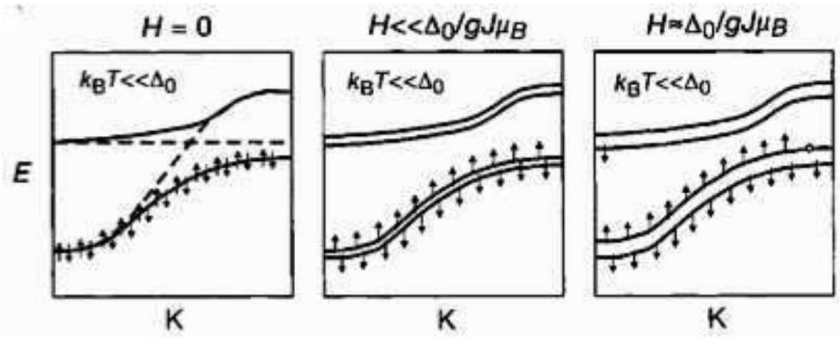


Figure 3.3: Schematic band picture of a Kondo insulator, showing how a magnetic field can drive a metal-insulator transition [10].

Kondo insulators are heavy electron systems in which the liberation of mobile charge through Kondo effect give rise to a filled heavy electron band in which the chemical potential lies in the middle of the hybridization gap. At high temperatures Kondo insulators metals with local moments with classic Curie susceptibilities, but at low temperature, when Kondo effect take place, the conductivity and magnetic susceptibility drops to zero [39]. This kind of materials can be understood as "half filled" Kondo lattice in which each quenched moments liberates a negatively charged heavy electron providing each magnetic ion with an extra positive charge. There are three good reason that support this key of lecture:

1. each Kondo insulator has its fully itinerant semiconducting analogue. For example $CeNiSn$ is iso-structural and iso-electronic with the semiconductor $TiNiSi$ containing $Ti_4^+$ ions with the $5f$-electrons entirely delocalized.

2. Replacing magnetic ion with iso-electronic non-magnetic ion is equivalent to doping.

3. The magneto-resistance of Kondo insulators is large and negative and can be closed by physically accessible fields.

other effects are not well understood within this picture:

1. The apparent disappearance of RKKY magnetic interaction at low temperature.

2. the nature of metal insulator transition induced by doping.

### 3.1.2 Heavy fermion superconductivity

Since the discovery of **heavy fermion superconductivity** [59] it was clear that the driving process of this phenomenon couldn't be the electron-phonon interaction for the pair creation. It can be understand easily by the integrated $C_v/T$ curve, which represents the entropy, which matches well with

the corresponding area for the normal phase of superconductivity :

$$\int_0^{T_c} dT \frac{(C_v^s - C_v^n)}{T} = 0 \tag{3.1.1}$$

since the normal state of entropy is derived by the $f$-moments. This means that the same degrees of freedom are involved in the development of the superconducting state. **Heavy fermion superconductivity** develops out of coherent, paramagnetic heavy Fermi liquid, so heavy fermion superconductivity can be said to involve the pairing of heavy $f$-electrons. A confirmation of this theory comes from the London penetration

$$\frac{1}{\mu_0 \lambda_L^2} = \frac{ne^2}{m^*} \ll \frac{ne^2}{m} \tag{3.1.2}$$

that is $20 - 30$ times longer than in normal superconductors [17], this reflects the large enhancement in effective mass.

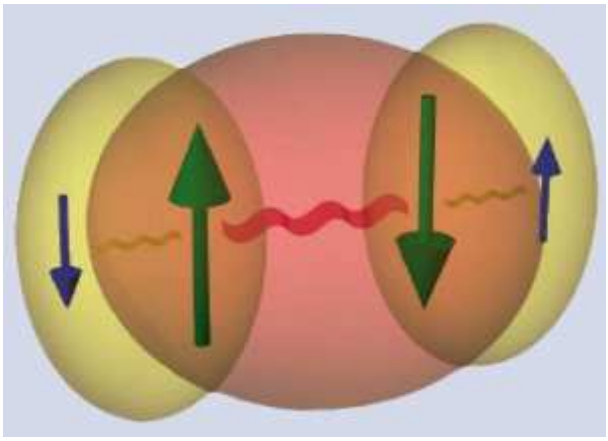

Figure 3.4: spin Cooper-pair (blue) coupled by a magnetic mechanism involving localized spins (green) [3].

The **microscopic model**: the classical theory of heavy fermion superconductivity treats the heavy electron fluctuation as a Fermi liquid with antiferromagnetic interaction among their quasiparticles, Fig. 3.4. Antiferromagnetic spin fluctuation are the driving force for this type of superconductivity [57, 47, 48], they drive an attractive BCS interaction in the $d$-wave superconductivity. This picture is consistent with the comparison of the energy scale of the RKKY interaction and Kondo interaction in Fig. 3.5, the RKKY

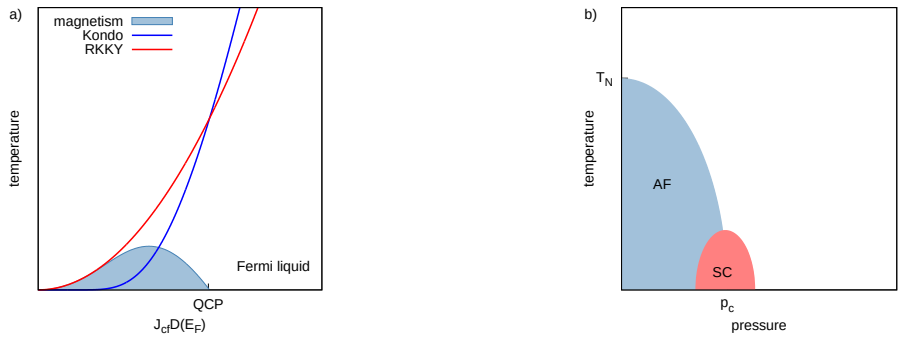


Figure 3.5: a) comparison of the energy scale of the RKKY and Kondo effect in function of the temperature. The appearance of superconductivity in the region where the RKKY interaction dominates on the Kondo effect confirm the picture of the pairs creation mediated by magnetic interactions. b) Phase diagram in function of pressure and temperature of a standard heavy fermion compound, [courtesy of Cornelius Strohm].

interaction tends to order the magnetic moments on one side, and the Kondo interaction tends to quench the moment of localized f-electron on the other side. The critical temperature of the RKKY interactions is scaled by the square of the exchange strength between the f- and the conduction-electrons and the density of states at the Fermi level: $T_{RKKY} \propto J_{cf}^2 D(E_f)$, but the Kondo temperature is exponentially dependent on $J_{cf}$: $T_K \propto e^{-(D(E_f)J_{cf})^{-1}}$. With the enhance of temperature these leads to the suppression of the long range magnetic order.

In other compound like $CeCu_2Ge_2$ and $CeCu_2Si_2$ the superconducting dome extends far beyond $P_c$, Fig. 3.6. One current idea is, that the second dome may have its origin in critical valence fluctuations arising close to a valence QCP at $P_v$.

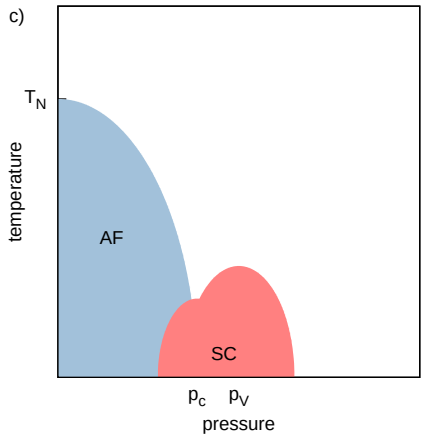


Figure 3.6: Superconducting phase with two critical pressures related to antiferromagnetic fluctuations ($p_c$ ) and valence critical fluctuations ($p_V$) [courtesy of Cornelius Strohm]

There isn't a full theory about these compounds, more experimental data are required for further theory development.

### 3.1.3 Quantum criticality

Many heavy electron systems can be tuned, with pressure, chemical doping or applied magnetic field, to a point where their antiferromagnetic ordering temperature is driven continuously to zero to produce a **quantum critical point** [20, 66, 46, 60, 61, 19]. The transformation in metallic properties, often referred to as non-Fermi liquid behaviour, that is induced over a wide range of temperatures above the quantum critical point (QCP), with the tendency to develop superconductivity near this singularity has given rise to a resurgence of interest in heavy fermion materials.

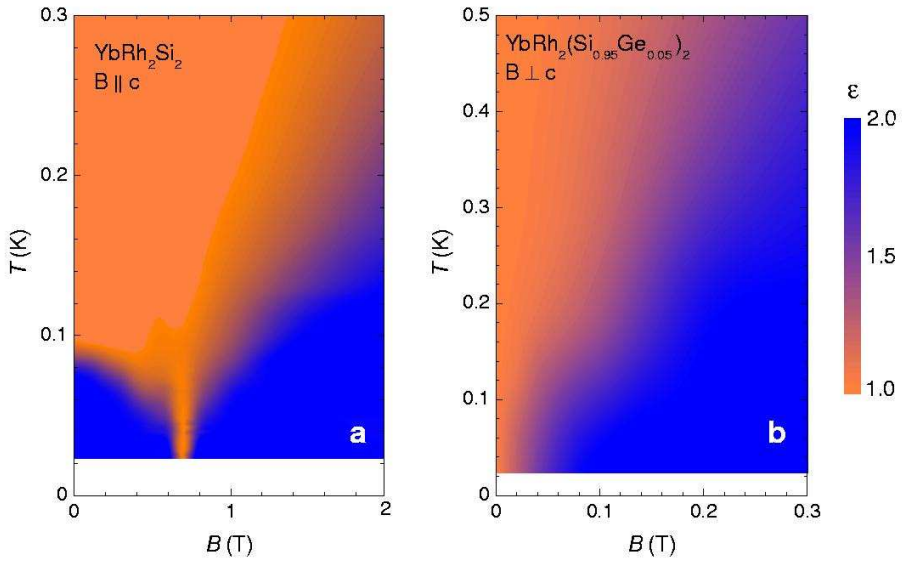


Figure 3.7: Quantum criticality in $YbRh_2Si_2$, a material with a $90mK$ magnetic transition that can be tuned continuously to zero by a modest magnetic field. The graph is colored with the logarithmic derivative of resistivity $d \ln \frac{\rho}{d} \ln T$ [38].

There are two kind of QCP:

1. **Soft** quantum critical systems are moderately well described in terms of quasiparticles interacting with soft quantum spin fluctuation created by spin density wave instability. Theory predicts a $\sqrt{T}$ singularity in the low temperature specific heat coefficient:

$$\frac{C_v}{t} = \gamma_0 - \gamma_1 \sqrt{T} \tag{3.1.3}$$

2. In **Hard** quantum critical heavy fermion many aspects of physics suggest the break-down of the Kondo effect associated with a relocalization of $f$-electrons into ordered local moment beyond the QCP. Their $Cv$ is:

$$\frac{C_v}{t} \sim \frac{1}{T_0} \ln \left( \frac{T_0}{T} \right) \tag{3.1.4}$$

The main difference between a classical and quantum criticality is the replacement of the temperature with magnetic field or pressure as a tuning parameter, Fig. 3.8.

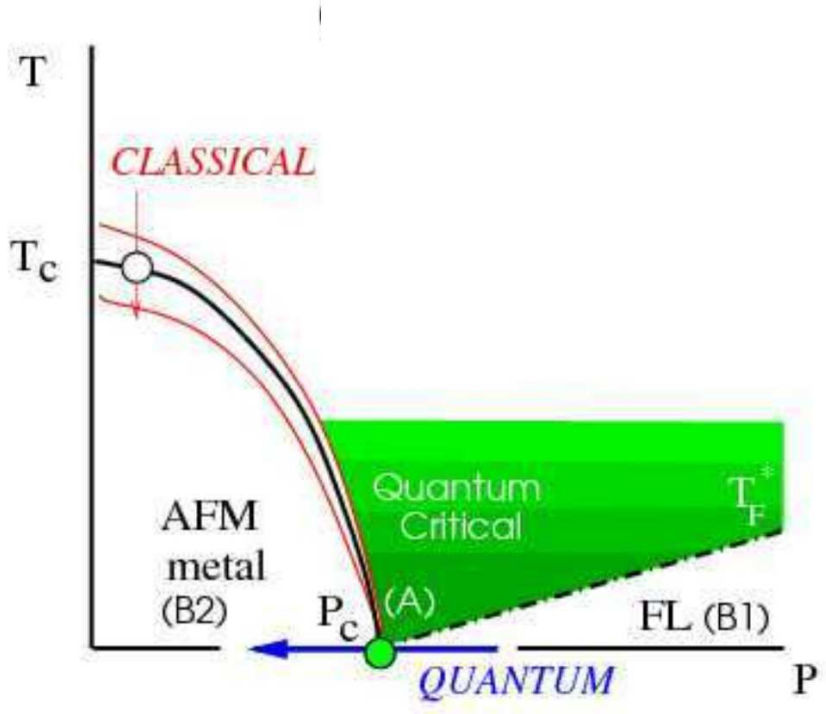


Figure 3.8: example of quantum critical heavy fermion, with a anti ferromagnetic phase **B1** and a paramagnetic Fermi liquid phase **B2**.

To investigate the physics of these compounds multi-extreme condition experimental set-up are needed, we said before that the quantum critical point can be achieved by the application of pressure, field or chemical doping. Today a system that combine pressure, high field and cryogenic temperature needed to achieve the QCP is lacking, this leads to part of my work: the design of an high pressure cell for a combined system of high pressure, pulsed field and cryogenic temperature for X-ray absorption studies at ID24 - ESRF.

## 3.2 Conclusion

In this chapter an overview on strongly correlated electron systems was given. In these systems the impossibility to describe their behaviour with a non interacting electron model leads to different and not always well understood properties. Then we focused on heavy fermion compounds, in particular on their superconductivity properties and quantum critical points.

# Chapter 4

# Miniature Tunrnbuckle cell

This part of the work describe the analysis of the problem, the design, realization, commissioning and working demonstration of a plastic diamond anvil high pressure cell made for X-ray absorption studies in pulsed magnetic field up to 30 T and at cryogenic temperature. The Diamond Anvil Cell (DAC) has been invented by Charlie Weir in NBS laboratory in 1958 for infrared studies [15]. It mainly consist in 2 diamonds facing themselves with a gasket with a hole in the middle to contain the pressure medium and a sample to be studied.

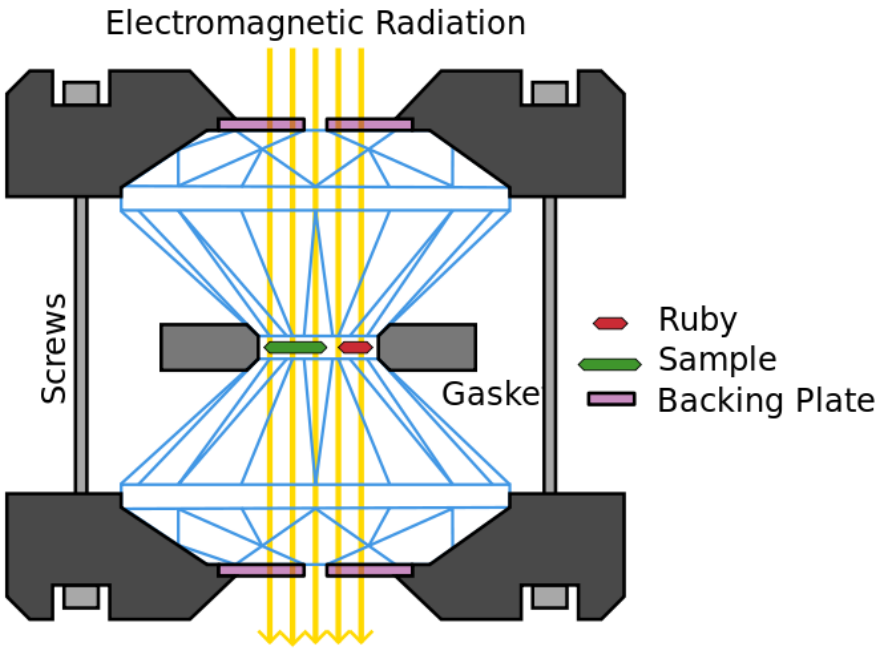


Figure 4.1: simple representation of Diamond Anvil high pressure Cell - DAC. There are all the necessary elements: 2 facing diamonds, a gasket to keep the pressure, a sample to be squeezed, a ruby for pressure measurements and a pressure medium to transmit hydrostatic pressure [4]

The working principle of the DAC is $P = \frac{force}{surface}$, in this cells is coupled the application of a screw-driven force with a small application surface (culets have diameter from $1mm$ to $150\mu m$). The conical shape well fits this purpose: it provides a sort of pressure "amplification". To achieve the $GPa$ range ultrahard material are usually used, the best candidate for this purpose is the Diamond: it's the hardest known material and it's transparent, both for X-ray and for visible light.

This kind of cell opened new opportunities for earth as well as solid state science: the possibility to study material under pressure with optical investigation opened a new world for physics [15]. It could be made a long story on DAC, ref [15] is an exhaustive article.

The DAC required in our experimental set-up has to face different problems:

1. fit into the small diameter of the cryostat inside the coil.
2. Eddy current heating in any metallic part
3. Forces due to the interaction of eddy currents with the applied field
4. X-ray transparency at relevant edges
5. possible contamination of spectra by Bragg diffraction from the diamond anvils.

All simulation reported here were made with python software written by myself.

## 4.1 Magnetic Field profile

The first approach to the problem has been a simulation on working condition witch the cell will suffer, it will be plumbed into a variable magnetic field whose temporal profile is known from Toulouse measurement, Fig.4.7 . The coil is a cylinder with inside radius of 11 mm, outside radius of 67 mm and length of 74 mm. The simulation of the field came from a discretization of the cylinder as superposition of spires. The magnetic field generated in the coil from a current $I$ along a spiral is:

$$d\vec{B} = \frac{\mu}{4\pi}\frac{\vec{dl} \times \vec{r}}{|\Delta r|^3} \tag{4.1.1}$$

with $\vec{dl}$ the local segment of the spire, $\vec{r}$ the distance from the spire and $\mu$ the dielectric constant. The geometry (symmetry) of the problem suggests to take into account only the component of the field parallel to the coil, the simulated axial and radial field profile are shown in Fig 4.2

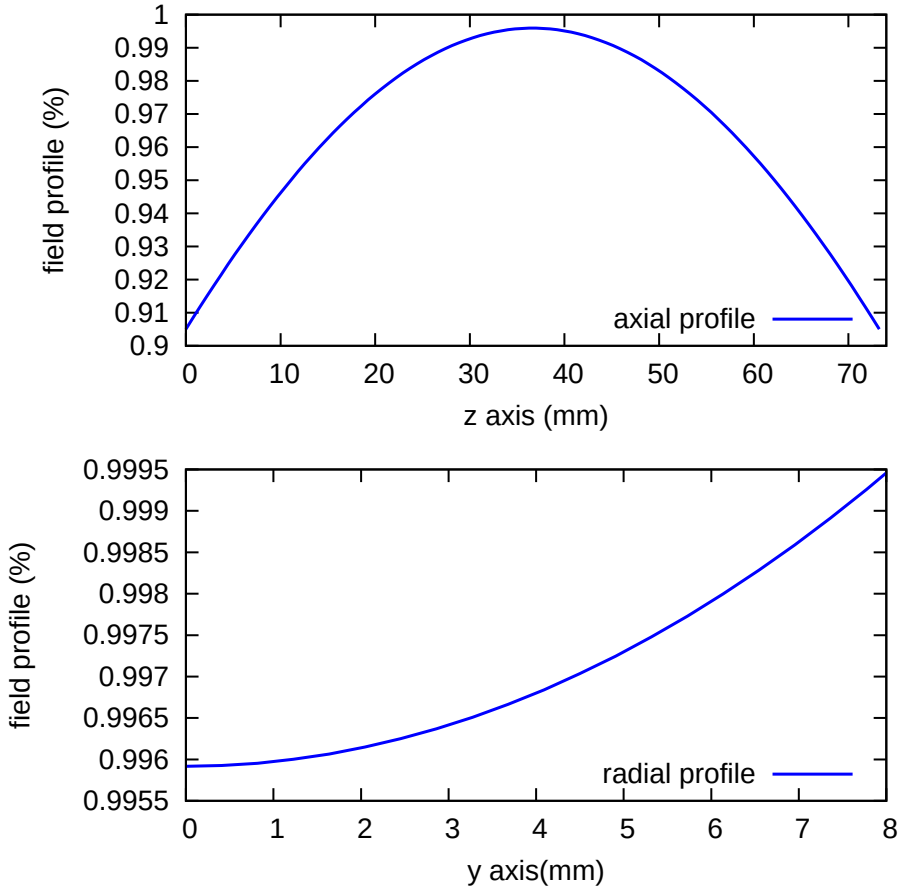


Figure 4.2: calculated axial and radial field profiles.

Based on this simulation I have renormalized the magnetic field profile taken from Toulouse measurements for the heating and force simulation.

## 4.2 Temperature and force simulation

A metallic cylinder inside a variable magnetic field will experience an electromotive force $\epsilon$ given by the Lenz law:

$$\epsilon = -\frac{\partial \Phi_B}{\partial t} \tag{4.2.1}$$

with $\Phi$ the flux of the magnetic field inside the cylinder: it causes a current I inside the metal. This leads at two consequences: generation of heat due to the Joule effect and interaction of the induced current with the applied field. The Joule effect causes the heating of the cylinder and leads to a

change of the temperature dependent resistivity and specific heat. The heat $\dot{Q}$ developed by a metal body in a variable magnetic field is [28]:

$$\dot{Q} = -\frac{GV\dot{B}^2}{\rho} \tag{4.2.2}$$

with V the volume of the material, $\dot{B} = \frac{\partial B}{\partial t}$, $\rho$ the resistivity of the material, and a geometry factor G:

$$G = \begin{cases} \frac{\pi r^2}{8} \\ \frac{\pi(r_{max}^2 - r_{min}^2)}{8} \\ \frac{d^2K^2}{16(1+K^2)} \end{cases} \tag{4.2.3}$$

The first expression is for a disk, the second for a cylinder and the third for a rectangular conductor, with $d$ the thickness, $K = w/d$ and $w$ is the width. The force acting on a charge in a time varying magnetic field is:

$$F = qv \times B \tag{4.2.4}$$

with $q$ the charge of the electron, $v$ the velocity of the electrons and $B$ the magnetic fields. The force in axial direction is equal to zero because the cross product between $v$ and $B$ has no axial components in our system and the radial forces produced are balanced for the cylindrical geometry of the cell. The force experimented by the cell is only due to the interaction of the magnetic moment with the spatial variable magnetic field: a spire in a spatial variable magnetic field will experiment a force in the axial direction given by:

$$\vec{F}_z = IA\frac{\partial B}{\partial z} \tag{4.2.5}$$

with $IA$ the magnetic moment of a spire and $\frac{\partial B}{\partial z}$ the variation of the magnetic field in the axial direction.

The hypothetical cell used for simulations has a maximum diameter of 10 mm to be fit into the cryostat and, as explained before, there is a gasket between diamonds with a maximum radius of 4 mm due to diamond dimension. I've carried out first simulation based on this cell geometry with 3 common materials frequently used for high pressure applications.

### 4.2.1 Materials

The design has started with a deep analysis of **geometry** and **material** to be used for building the cell. Several material were taken into account for the cell body and gasket, in the following table are reported the value of resistivity and heat capacity of the material taken into account for the design of the cell. We carried out **heating** and **force simulation** for each material. In Fig. 4.3, 4.4 are reported the temperature dependence of **resistivity** and **molar specific heat** with interpolation for the materials taken into account for the simulation.

| **material** | **resistivity** $\mu\Omega$ | **heat capacity** $\frac{mJ}{molK}$ |
|---|---|---|
| $Ti$ | 0.020000 | 7.4938852 |
| $Cu$ | 0.000020 | 1.7544847 |
| $Rh$ | 0.000045 | 3.1282500 |
| $TiAl_6V_4$ | 1.469000 | 7.4938852 |
| $CuBe$ | 0.081800 | 1.7544847 |

Table 4.1: metals studied for the cell and gasket building, this data are for the initial condition: 2K. [11, 63, 65, 67, 52]

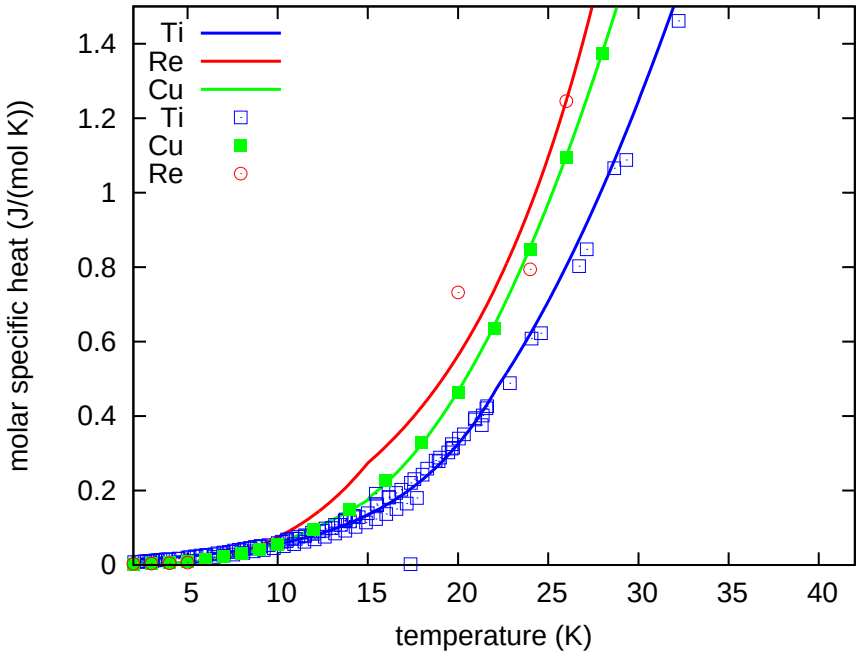


Figure 4.3: temperature dependence of the molar specific heat for Cu, Ti and Rh.[63]

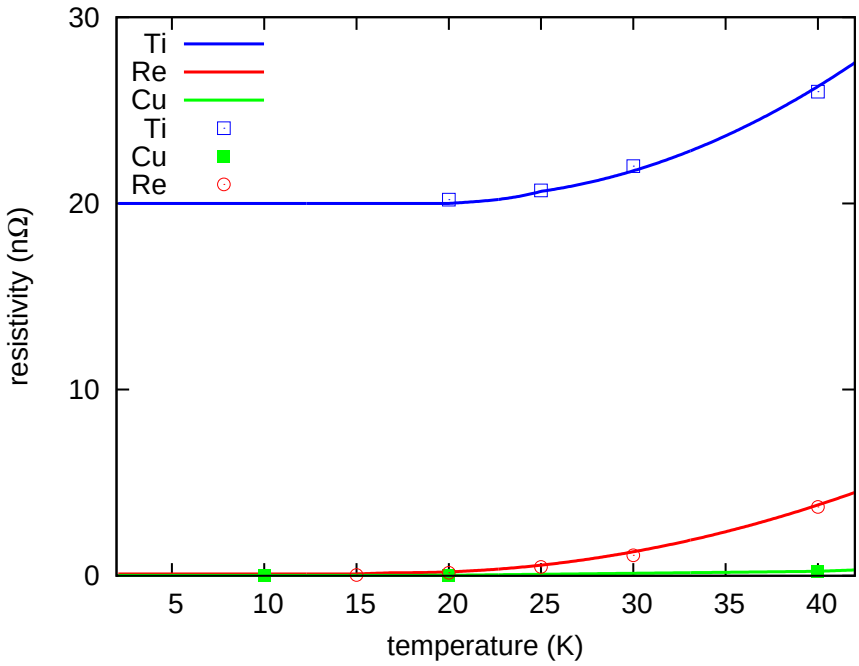


Figure 4.4: temperature dependence of the resistivity for Cu, Ti and Rh.[65, 67, 52]

With that functions I could write a python script for the calculation of the **current density**, **force** and **temperature**. A good figure of merit to determine the suitability of a material is the factor $\frac{1}{\rho c}$ where $c$ is the heat capacity of the cell or gasket. We can find the reason in the description of the temperature change:

$$\Delta T = \frac{\dot{Q}dt}{C_p(T)nmol} = \frac{GV\dot{B}^2dt}{\rho(T)C_p(T)nmol}$$

where $nmol$ is the number of moles, $C_p$ in the specific heat and $\rho$ is the resistivity where both, $\rho$ and $C_p$ are temperature dependent, Fig 4.5.

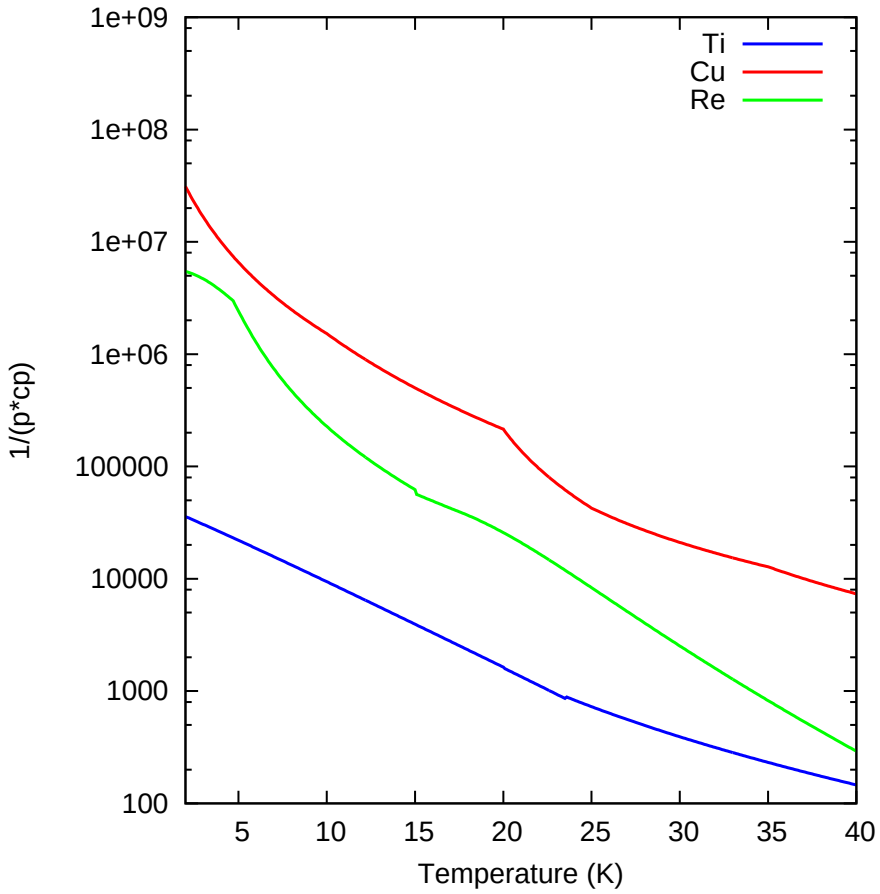


Figure 4.5: Factor $\frac{1}{\rho c}$ useful to determinate the best material for the cell construction. The edges in the lines arise from different interpolation functions for the resistivity and specific heat

Based on this simulation we carried out **temperature simulation development** for cell's heating for an hypothetical cell made of pure Titanium

or Copper, Fig 4.6

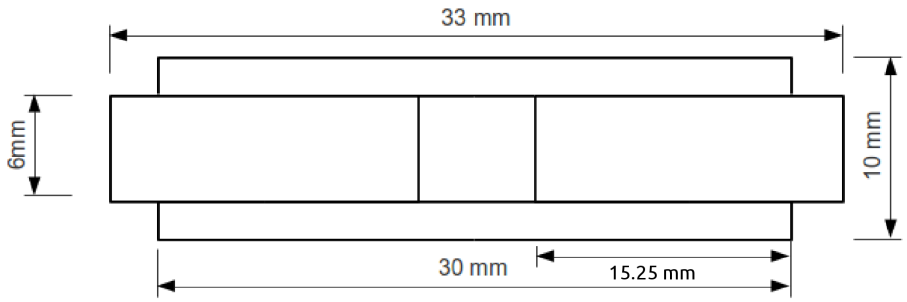


Figure 4.6: model of the cell used for the simulation

In Fig. 4.7 is reported the result of the temperature development of the prototype cell. The sharp increase of the temperature during the beginning of the pulse is due to the temperature dependence of the resistivity and the heat capacity as the fast increasing magnetic field.

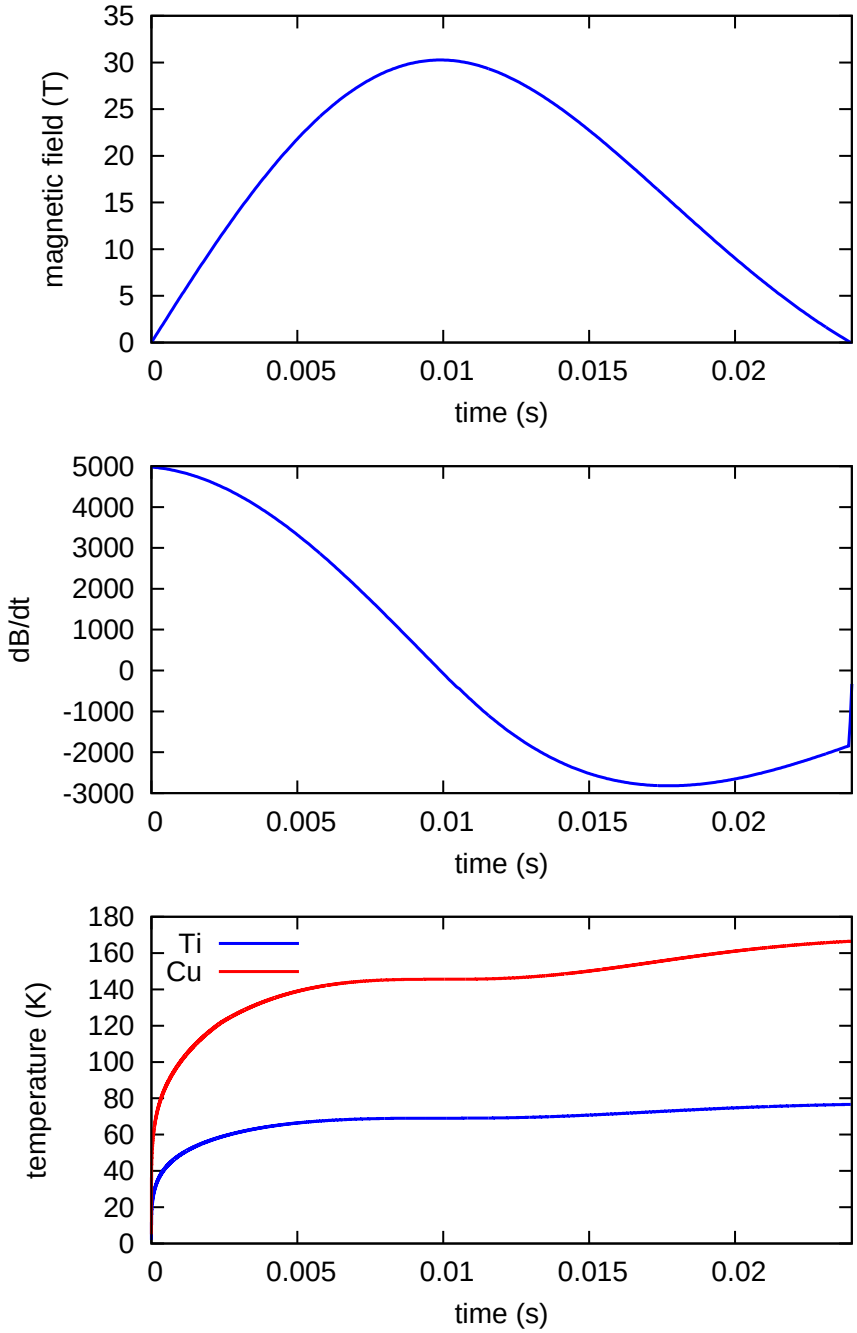


Figure 4.7: Temporal evolution of the pulse and its derivative, the third graph shows the temperature evolution of the cell during the pulse, this cells are made by pure Copper and Titanium.

At this point we realized that the best candidate was Titanium, we researched in literature different alloys made with this material and carried out similar simulation for two different alloys: $TiV4$ and $TiAl6V4$ both this

alloys are non magnetic, Fig. 4.8. In Fig. 4.9 is reported the force development in parallel direction for a $0.5mm$, $1mm$ and $3mm$ displacement of the cell.

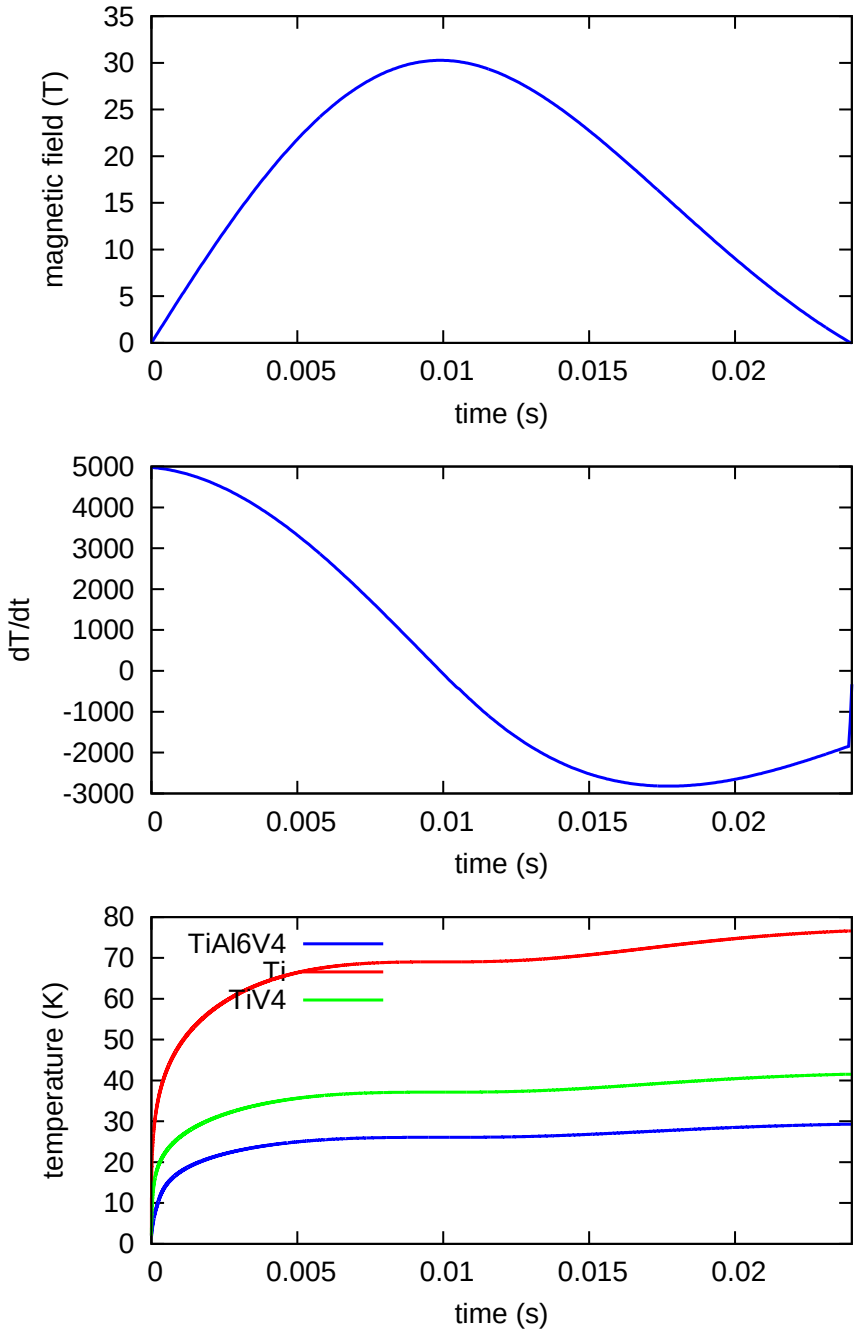


Figure 4.8: Temporal evolution of the pulse and its derivative, the third graph shows the temperature evolution of the cell during the pulse, this cell is made by Titanium Alloys. [11]

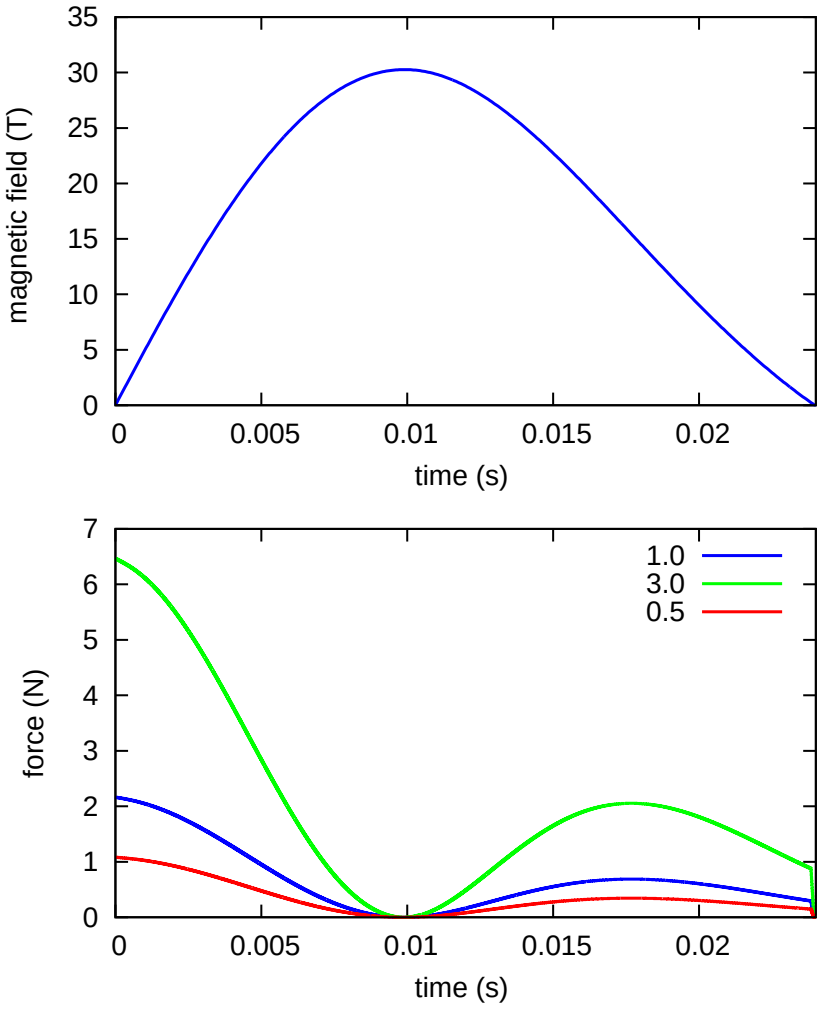


Figure 4.9: Temporal evolution of the axial force for 3 different displacements, 0.5, 1 and 3$mm$ for a $TiAl6V4$ cell.

From this simulation it's clear that a full body cell will not satisfy our task, we have an upper limit for heavy fermion compound studies of 6-8$K$ starting from a 2$K$ temperature. We decide to try a simulation with a 4 body divided part cell, Fig. 4.10.

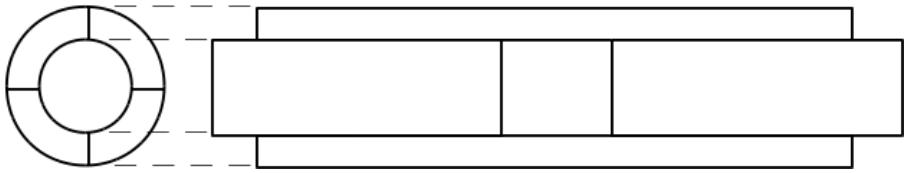

Figure 4.10: model of a cell, with an outer body divided in 4 sections.

and in Fig.4.11 are reported results. In the same picture is also reported

the heating of the gasket due to the heating flux coming from the cell through the two diamonds with a $Ti$ or $Cu$ gasket. The black line represent the same configuration with a $5mm$ of Vespel polymer between metal and diamond to avoid heating exchange between cell and sample.

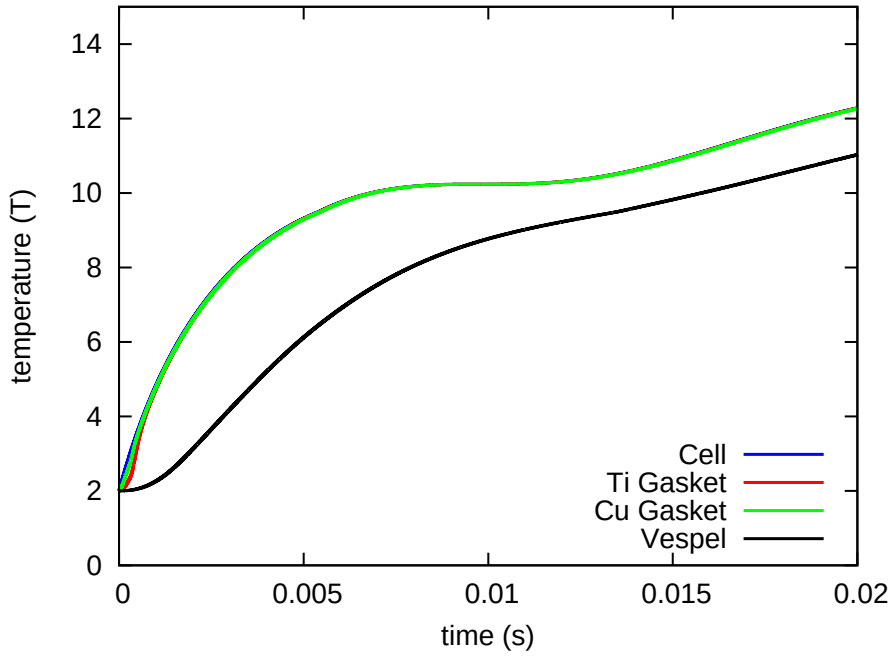


Figure 4.11: Gasket heating caused by the Cell. I used a configuration where the outer body of the cell of $TiAl6V4$ is divided in 4 sections to avoid eddy currents along the circumference of the cell. In the graph are reported the heating of a $Ti$ an $Cu$ gasket due to heat flux through the diamonds from the cell. The black line represent a simulation with diamonds isolated from the cell by 5 millimeter of VespelSP1 a low thermal conductive polymeric resin. I took into consideration the surface contact thermal resistivity under pressure for the thermal conductivity of the insulator, I didn't considered the thermal conductivity of the diamonds for previous the simulation. [68]

Starting from this simulation it is clear that a cell made in metal can't in any case satisfy our goal, there is another problem to be faced: the gasket. We have repeated the temperature simulation on the eddy current heating for $TiAl6V4$ gaskets of different diameters. 4.12.

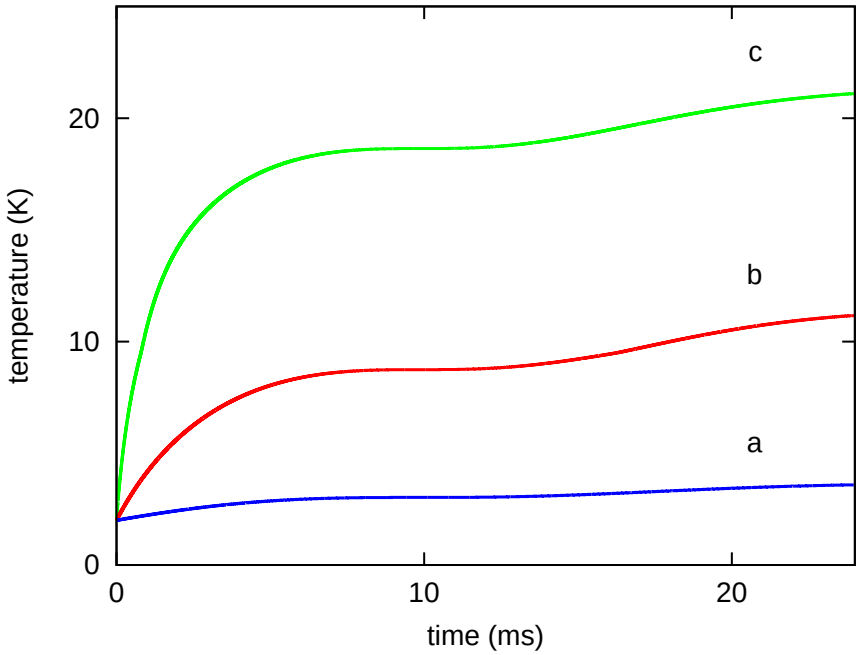


Figure 4.12: temperature evolution for $TiAl6V4$ gaskets with different diameters: **a** $0.45mm$, **b** $1.5mm$ and **c** $4mm$ gasket.

At this point it is clear that a full-body metal cell and a self supported full-metal gasket can't meet the requirements of our project. We decide to design a brand-new plastic cell after this simulation.

## 4.3 Design

The principle of the DAC were introduced in the previous section, but some elucidation on DAC's working are required to understand properly miniaturization process problems. The pressures that this kind of cell could achieve in priciple arises to hundreds of GPa, far over compressive and tensile stress that metal could stand. pressure keeping inside the hole is possible for metal indentation before pressure applying in order to create a biconical guide for diamond ended with 2 parallel plates, Fig. 4.13. In plate's centre will be drilled a hole where will be placed the sample, ruby and pressure medium, the diameter of the hole is usually 1/3 of the culet dimension. Starting from this point it's clear that a small diamond misalignment or unparallelism end

up with an hole flowing out of culets. It is clear that diamonds must be centred and aligned to achieve this task: in normal cell there are a set of screws for diamond settings.

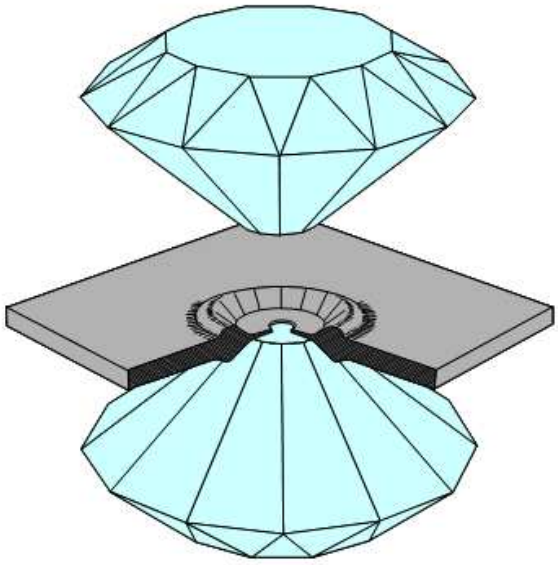

Figure 4.13: simple view of gasket indentation and placement [6].

Few groups in the past had worked on cell miniaturization to fit magnet or cryostat [12, 22, 26, 31, 33, 45, 69] with many different ideas to keep the possibility of diamonds alignment. We realized that it was impossible in our case to have any kind of diamond adjustment screw inside the cell for dimension problem and over that plastic screws for pressing plates weren't a good option for material properties and machining problems. We look into literature to have an inspiration and we discover the turnbuckle concept of Tozer [22].

Figure 4.14: turnbuckle tensor [4].

"The turnbuckle is a device for adjusting the tension or length of ropes, cables, tie rods, and other tensioning systems. It normally consists of two threaded eyelets, one screwed into each end of a small metal frame, one with a left-hand thread and the other with a right-hand thread. The tension can be adjusted by rotating the frame, which causes both eyelets to be screwed in or out simultaneously, without twisting the eyelets or attached cables.[4]", Fig. 4.14. The main feature of this concept is the self sustaining body that works as a screw itself. We overturned the concept in pressure than in tension, than once the diamond are in contact it's possible to adjust the pressure by keeping the two screws and rotating the body, over that once found a good position for diamonds it's possible to align them before squeezing the cell. In Fig 4.15 is represented the cell, the lateral and angular alignment are provided by cell construction: 2 flat surface at both sides of the thread assure the centing of the diamond supporting backplate. On this surface is mounted the diamond, it's a nano-crystalline laser machined diamond,

the round surface give us the possibility to fix their lateral position with a fiberglass sleeve. Within a certain machining tolerance angular alignment can always be achieved through the rotation of the diamond [27] this assure the possibility to align diamonds.

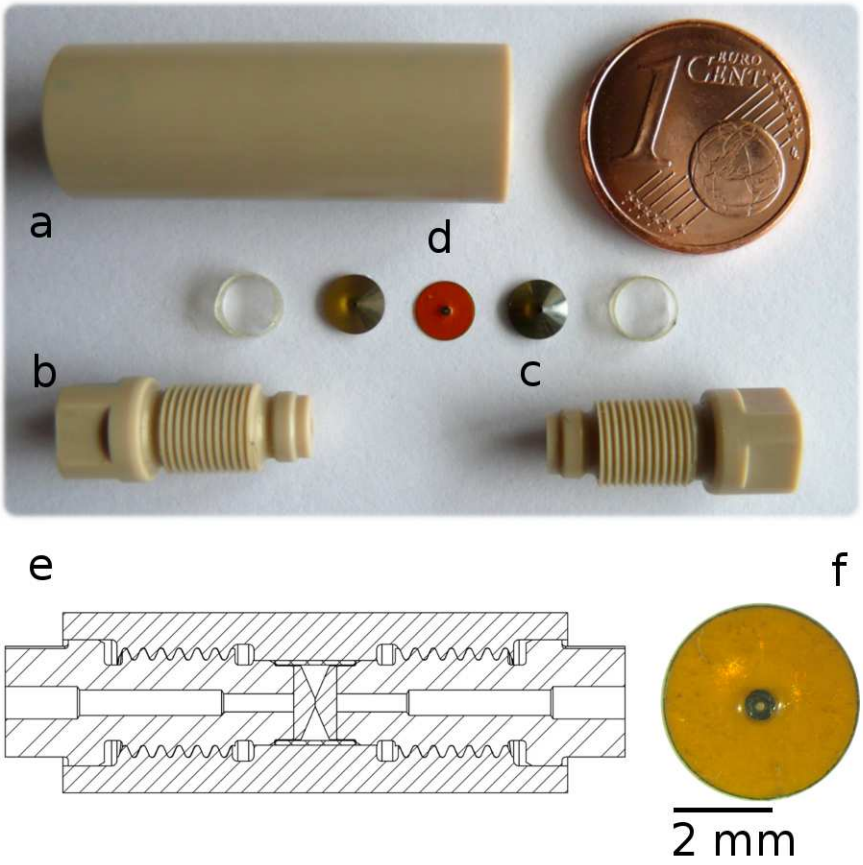


Figure 4.15: miniature plastic turnbuckle high pressure cell. **a** body, **b** left culet, **c** right culet, **d** from left to right: sleeve, diamond, gasket, diamond, sleeve, **e** cross-section and **f** gasket. [22, 44]

### 4.3.1 Gasket

Previous simulation showed than a self-sustaining metal gasket doesn't satisfy our needing, we tried a lot with a non metallic gasket [29, 22, 44] made with boron-epoxy mixture but we understood at the end that the small renaming misalignment of diamonds due to machining precision caused frequent failures of this technique. Then we tried to substitute the inner part with a $TiAl6V4$

pre-indented central part externally supported with a ring of Kapton, Fig 4.15 **f**, 4.16. We decided the inner gasket radius based on 2 parameters: the heating by induced current, Fig 4.12 **a**, and the possibility to make it externally sustained by a ring of Kapton. We choose Kapton foil for its good tensile strength [44] and in consequence its ability to absorb large hoop stress created by the inner gasket.

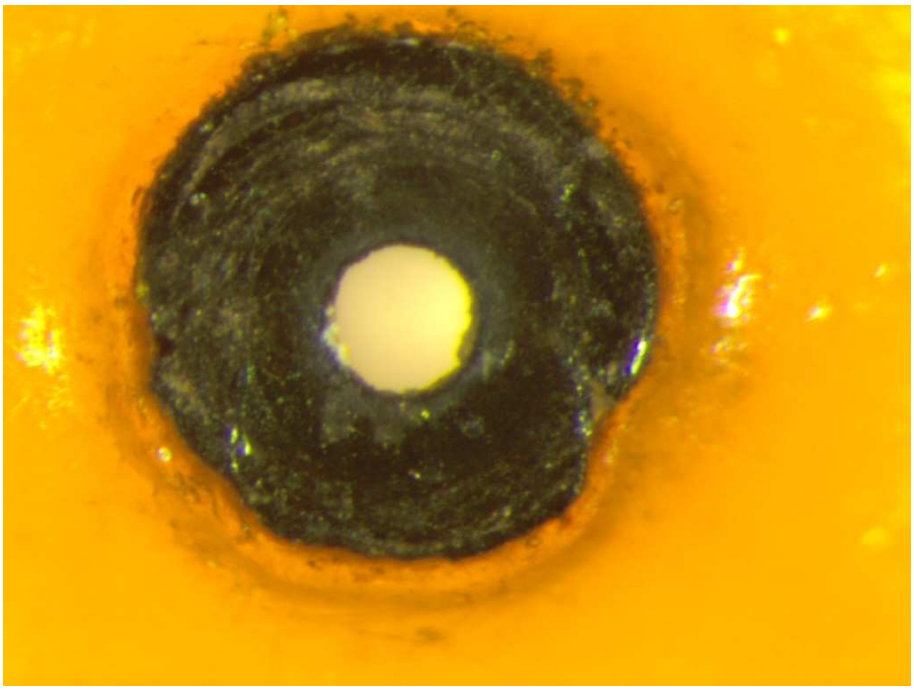

Figure 4.16: metallic inner part of the gasket. It can be seen that the external supporting Kapton part is slightly deformed by hoop stresses of the inner metallic ring.

### 4.3.2 Plastic material

Many different non conductive high-performance X-ray resistant plastic are now available on the market, we choose PEEK [4] for the first prototype of this cell for its well known machining properties and good tensile strength, 90-100$MPa$, that allowed us to reach a pressure of 5-6$GPa$ without damage to the cell. We have machined the standard one in Tecamax with its exceptional tensile strength of 207$MPa$ [7] will allow us to reach 10-11$GPa$.

## 4.4 Results

To demonstrate the cell working behavioured we took a sample of Crocoite $PbCrO_4$. This crystal change colour in transmission from orange at $0GPa$ to deep blue $3.5GPa$ [14]. To load the cell has been used a $4mm$ diameter $Cu$ gasket with a thickness of $50\mu m$. As pressure medium was used silicon oil and the ruby for pressure measurements were placed near the sample. In Fig. 4.17 we can see the changing in transmission properties of the sample under pressure, below the picture of the sample we show the ruby fluorescence spectrum used for the pressure determination.

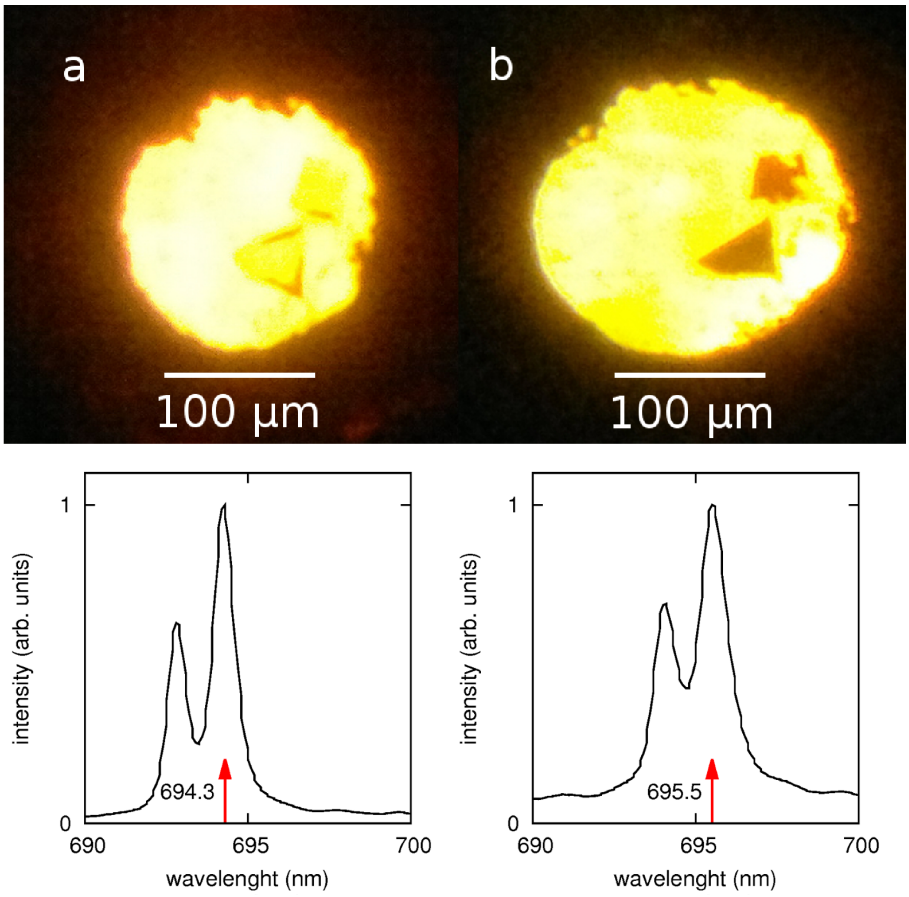


Figure 4.17: color change of a sample of crocoite $PbCrO_4$ under pressure.**a** sample at 0.10 GPa, **b** sample at 3.52 Gpa. [14]

After this proof we tested the cell inside the magnet and the cryostat. A disk of $80\mu m$ $Cu$ foil has been placed inside the cell gasket to test the

vibration induced in the structure by the interaction with the magnetic field. After a week of debugging an encouraging result is reported in Fig. 4.18. The bad resolution of adsorption spectra taken with the cell compared to the foil one in due to the X-ray scattering of diamond.

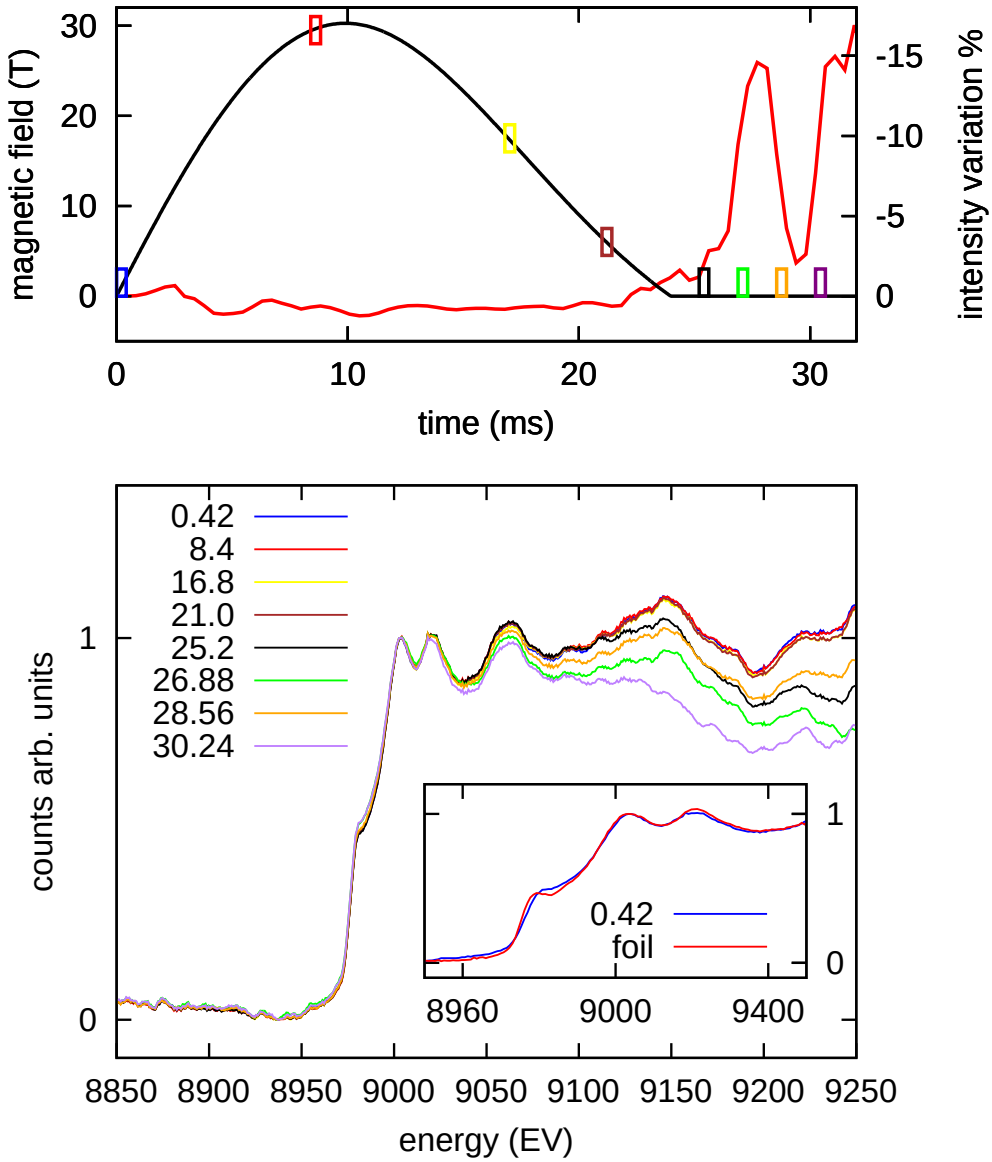


Figure 4.18: selected absorption spectra of a $80\mu m$ disk $Cu$ foil inside the cell, this is the normal dimension of a sample used in absorption study. The intensity variation during the field pulse is in the percent range, as can be seen in the $Cu$ absorption spectrum the acquisition windows inside the pulse corresponds to a good spectrum. The acoustic interaction with the system starts to be important after the end of the pulse. The acquisitions are made sequentially every $0.42ms$. The small graph shows the comparison between a copper spectrum inside and outside the cell. It is clear that the small angle scattering from the diamonds leads to a reduced resolution.

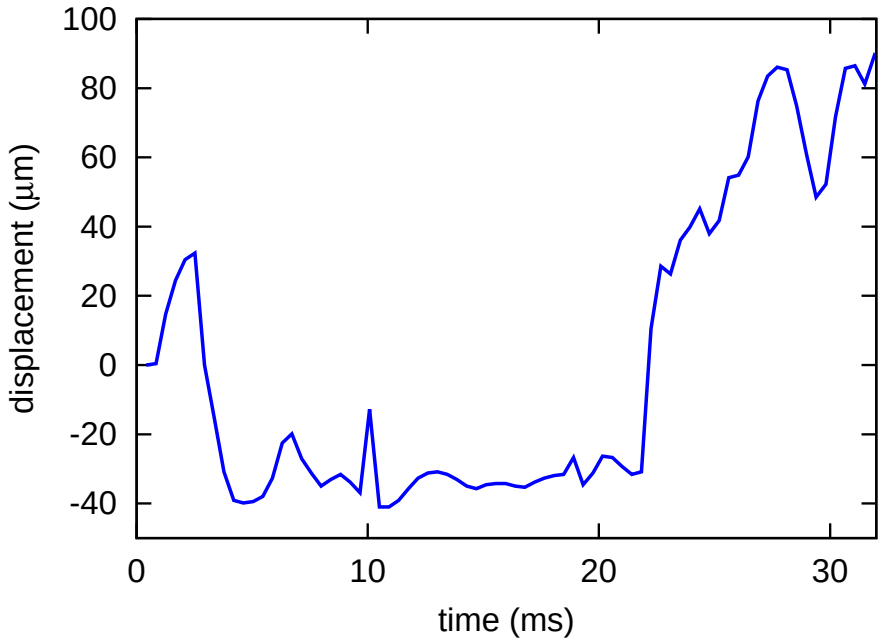


Figure 4.19: displacement of the beam inside the cell during the pulse. Tests have shown that the major oscillation mode is the vertical one. Vertically the beam has a Gaussian profile with a FWHM of about $100\mu m$. Starting from this assumption it is possible to estimate the vertical displacement of the beam during the field pulse.

In Fig. 4.20 is reported the size of the beam used for measures.

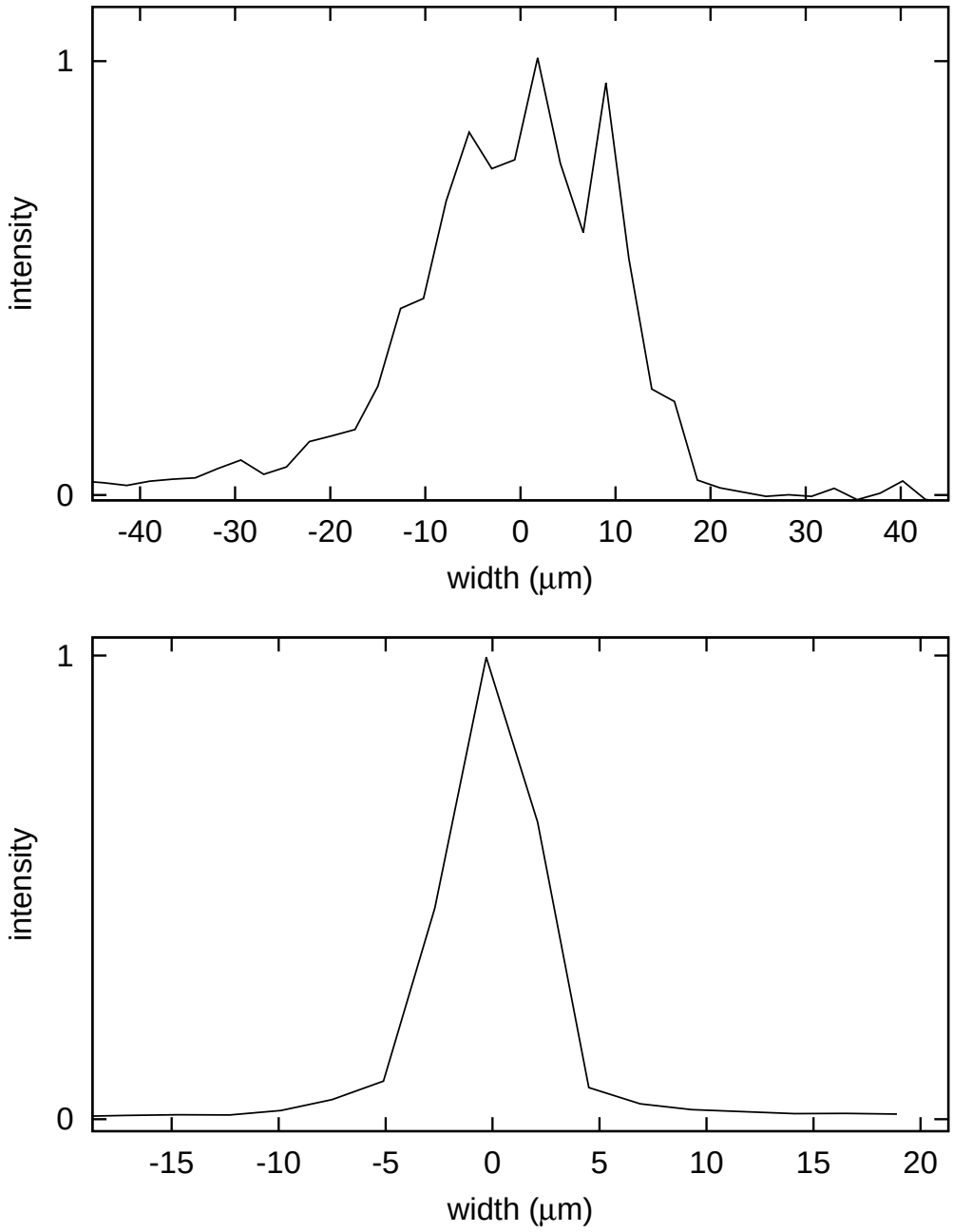


Figure 4.20: vertical (top) and horizontal (bottom) beam profiles.

To determinate the displacement of the beam I used the intensity variation of the total photon counts: when the beam moves from the original position there is a variation of the total intensity because the titanium gasket absorb all the incoming radiation for its thickness. Starting from the Gaussian profile of the beam is possible, in first approximation, to connect

the intensity variation with the geometrical position. Fig. 4.18 and 4.19 are the proof that is possible to use this high pressure cell with the cryostat in the centre of the magnet. The technical part is ready for further HFC studies.

## 4.5 Conclusion

In this chapter has been designed, developed, lab commissioned and tested a miniature plastic turnbuckle high pressure cell. After the working proof the cell has been tested inside the experimental set-up composed of a pulsed magnet and a cryostat. The results clearly shows that for the first time is possible to use X-rays for absorption studies in a multi-extreme set-up. This set-up is useful for Heavy Fermion Compound studies because the possibility to tune the material properties via pressure and field application instead of temperature application could allow us to reach QCP that now are not investigable for the extremely high field required to reach them. The data that will be gained from this further studies will contribute to carry on the development of the lacking theory of HFC behaviour at low temperature.

# Chapter 5

# Temperature dependence of the valence in the Heavy Fermion Compounds $YbCu2Si2$ and $YbRh2Si2$

One of the major issues not fully resolved in the study of rare-earth (RE) intermediate-valence (IV) compounds is the interplay between magnetic and valence instability, especially when the system is driven by the application of an external parameter as pressure towards a magnetic quantum critical point (QCP), where strong spin and/or valence fluctuations are expected to arise. Especially noteworthy are the IV REM2 X2 (where RE=Ce,Yb, M=transition metal, X=Si,Ge) compounds widely studied during the past decades owing to the interesting physical properties they exhibit as heavy fermion compounds, different types of magnetic order, superconductivity and non-Fermi liquid behaviour. All these phenomena are based on the non-integer occupancy of the 4-f orbital and to the competition among the significant energy scales of these systems: crystal electric field effect (CEF), Kondo effect and Ruderman-Kittel-Kasuya-Yoshida (RKKY) interaction [9]. In the next section will be presented the temperature dependent valence transition analysis of 2 HFCs $YbCu2Si2$ and $YbRh2Si2$.

## 5.1 Spectra

This is a preliminary study made in preparation of an user experiment with the experimental set-up explained into this work, the data taken will be used as reference for the study of magnetic induced valence changes. The experimental work has involved the absorption study around the $L3$ edge of $Yb$ that exhibits two white line peaks, separated by $7eV$ between the ion $Yb^{2+}$ and the $Yb^{3+}$. These compounds are metallic and electronic shell structure of the $Yb$ atom changes from $[Xe]\ 4f^{14}6s^2$ of the free atom to a superposition of $[Xe]\ 4f^{14}$ for $Yb^{2+}$ and $[Xe]\ 4f^{13}$ for $Yb^{3+}$. This 2 ions have a particular interest because $Yb^{3+}$ is magnetic and $Yb^{2+}$ is not, I have summarized before why the magnetic interaction is so important to understand HFCs physics. The energy separation between the white lines of these two ions is 7 eV, it is due to the broadening due to core-hole lifetime of $4.6eV$ convolved the experimental resolution of about $1.5eV$ and the two ion has a position of the $L3$ edge separated of $7eV$, this value is comparable with the width of the absorption line convolved with the experimental resolution. The two valence state are therefore not fully resolved and result spectra is shown in Fig 5.1. In the picture are reported two spectra taken at $15K$ and $295K$ of $Yb$ compounds: there is a clear difference that indicating a valence transition as function of temperature.

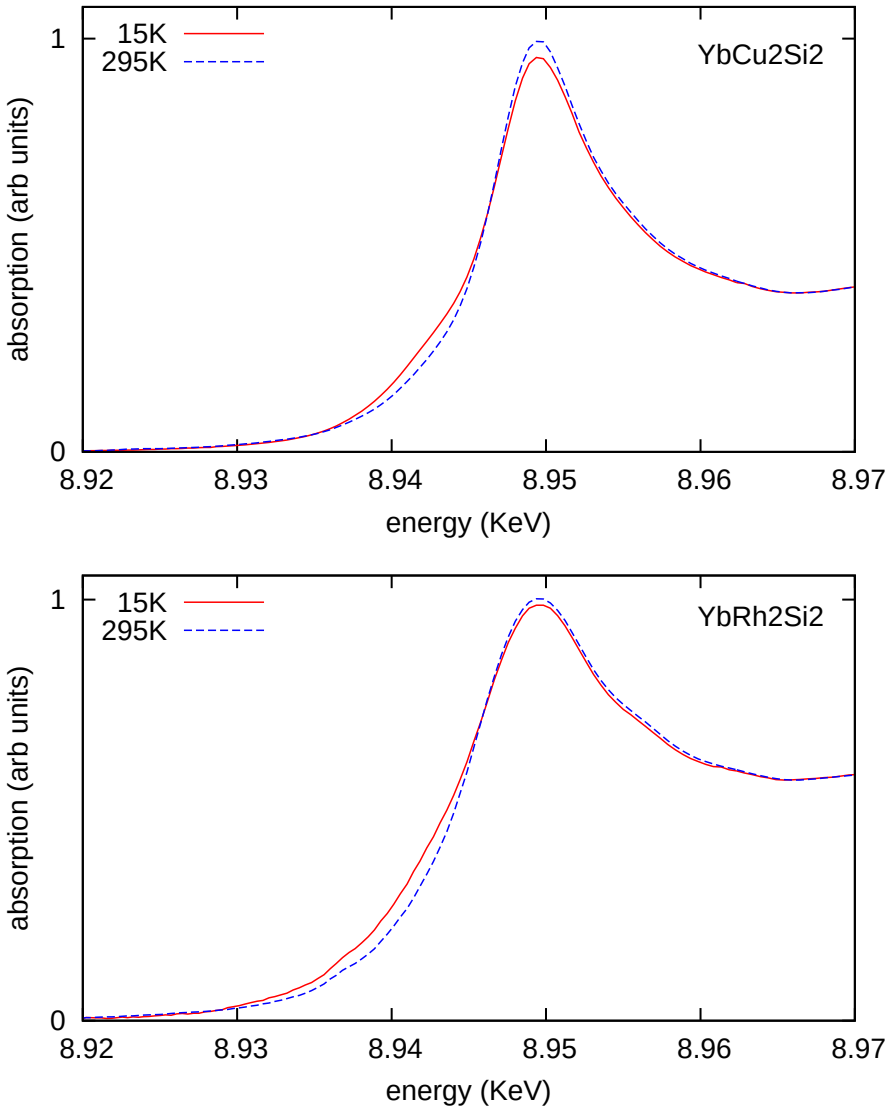


Figure 5.1: two superposed spectra of the $L3$ edge of $Yb$ at the $15K$ and $295K$.

The spectra are composed of a white line and a step-like function, the white line corresponds at localized state because the energy is near the bounding energy of the electron, the step-like function corresponds to extended state for the bigger remaining energy of the electron that became kinetic energy. The difference in energy between the $Yb^{2+}$ and $Yb^{3+}$ ion came from the different screening energy of the inner electronic shell, the electrons of the two different ions feels a different potential of the nucleus [25]. The $Yb^{3+}$ ion has the white line shifted at higher energy for the higher potential felt

by electrons.

Fig. 5.2 shows the difference between the $15K$ spectrum and the other $YbCu2Si2$ spectra as a function of temperature. The difference is enhanced by the temperature due to the immersion of more $4f$ electrons into the Fermi sea. The process is continuous without any jump.

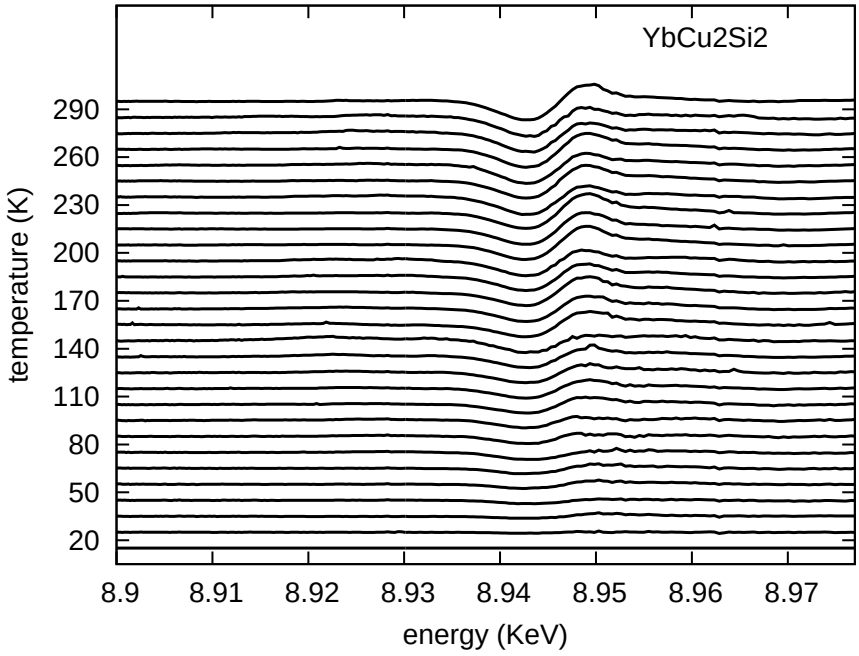


Figure 5.2: temperature dependent difference between the $15K$ and the $T$ $YbCu2Si2$ spectrum. As can be clearly seen by the difference graph, there is a continuous change in the spectra due to the valence change of the $Yb$ ions.

To analyse the spectra we use the following simple model: I approximate the localized state with a Lorentzian with a FWHM of $7eV$, as explained before this value comes from the convolution of the core-hole lifetime with the experimental resolution, and the extended states with an arctangent. Once fixed the ration between the Lorentzian and the step-like function by interpolate the spectrum at $295K$ with a single function is possible to fit the spectra with a linear combination of 2 prototype functions shifted by $7eV$ [70, 9, 62] corresponding to the $Yb^{2+}$ and $Yb^{3+}$ ions. In Fig 5.3 is reported one spectrum with the different interpolating curve.

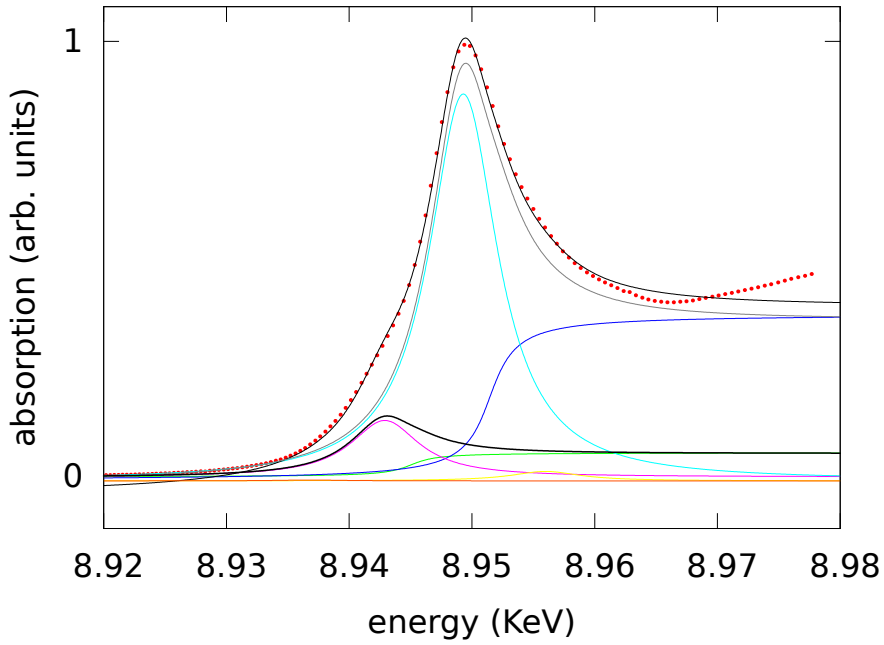


Figure 5.3: components used for the fitting function of a $15K$ $YbCu2Si2$ absorption spectrum.

From the linear combination of the function is possible to extract the valence of the compound:

$$v = \frac{2 * a_{Yb^{2+}} + 3 * a_{Yb^{3+}}}{a_{Yb^{2+}} + a_{Yb^{3+}}} \tag{5.1.1}$$

with $a_{Yb^{2+}}$ and $a_{Yb^{3+}}$ the amplitudes of the Lorentzians and $v$ the valence of the compound. In fig. 5.4 is reported the valence in function of the temperature of the two compounds studied obtained by the analysis explained before.

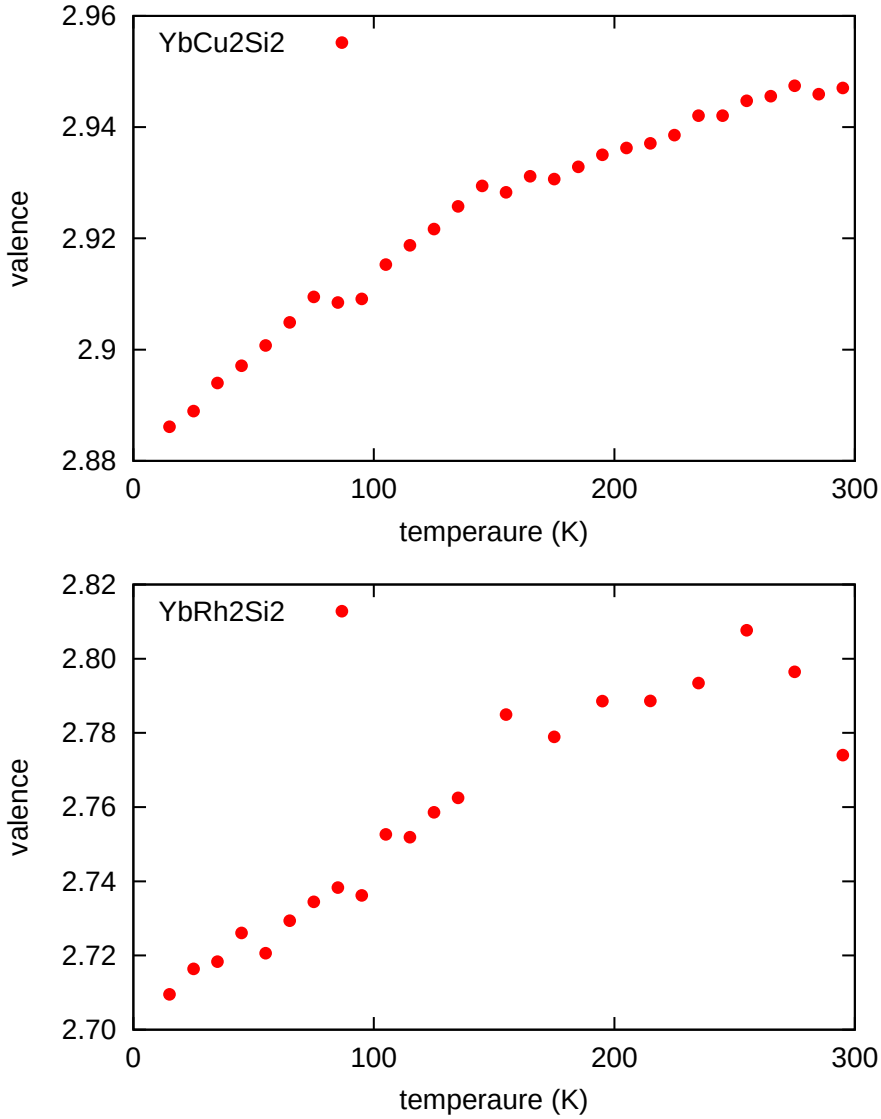


Figure 5.4: temperature evolution of the valence in $YbCu2Si2$ and $YbRh2Si2$, the values are in agreement with literature [9].

## 5.2 Conclusion

In this chapter we studied the temperature dependence of the valence of two mixed valence compounds $YbCu2Si2$ and $YbRh2Si2$ starting from absorption spectra. Results clearly shows the temperature dependence of the valence of $Yb$ ions, the two samples analysed are metallic and the $Yb$ ion assume a configuration of $Yb^{2+}$ or $Yb^{3+}$. This ions have an electronic structure of $[Xe]\ 4f^{14}$ for $Yb^{2+}$ and $[Xe]\ 4f^{13}$ for $Yb^{3+}$, this means that one $4f-$electron of the $Yb^{2+}$ ion leave the atom and became a member of the Fermi sea.

# Acknowledgements

Many people has to be thanked for the realization of my thesis. First of all Cornelius Strohm, my supervisor scientist at ID24, that followed me in every step of my work experiencing how an Italian student can be different from a German supervisor, and all the ID24 team (Sakura, Oliver, Carlo, Innokenti, Florian, Suresh and Deborah) that make me feel like in a family for all the time spent in Grenoble. Than I have to thank Giacomo Ghiringhelli that make this amazing experience abroad in one of the best place possible in the world to do science and provide me all the support needed by a student. A special mention goes to my family to have supported me for all this student's years, to bear me and to make me feel close also in another country. Than comes the second family: les Mesdemoiselles de Fontaine to have brought a stone in France from Tuscany, Je with her Venetian finesse, Mel with her dinner comparable to my Grandma ones and Giulia... just to be you, Giulia. To Visco and Ska, that I know that waits me outside with a goat on a leash or something even more stupid, I love you guys, with the bigger non-gay love possible, no, ok, maybe a bit gay. To "il Pisqui" and Luigi to have drunk so much Ceres and Beck's to pay my studies and to Francy, Omar and Norma to be great stoned collegues at Ol Muli. To Reddy, to be a spiritual guide of the "Gnagna". To all the Grenobloise crew: Pier, Gessa, Carlos, Clemens, Celine, Marta, Claudia "GRANDE GIOVA" and Armel to be great party and travel friends. To all the friends of the "Centro Zero" and in particular to Maurizio Bianzini, you make me most of the man that I am. Last but not the least to all other firends: Valentina, Ayu, Greta, Marina, Maria, Bat, Tom, Giulio and all the others.

# List of Figures

# Bibliography


[1] *http://internal.physics.uwa.edu.au/.*

[2] *http://www.esrf.eu/.*

[3] *http://www.uni-mainz.de/FB/Physik/AGAdrian/heavyF/heavyF.html.*

[4] Wikipedia. http://it.wikipedia.org/wiki.

[5] *www.lightsources.org.*

[6] *www.physics.buffalo.edu.*

[7] *High Performance Plastics.* iSmithers Rapra Publishing, 2005.

[8] L. Incoccia A. Bianconi and S. Stipcich. *XAFS and near edge structure: proceedings of the International Conference, Frascati, Italy, September 13-17, 1982.* Springer series in chemical physics, 1983.

[9] D. Braithwaite L. Paolasini R. Verbeni G. Lapertot 1 A. Fernandez-Paella, V. Baldent and J.-P. Rueff2. Valence instability of ybcu2 si2 through its quantum critical point. *Physical rewiew B*, 86:125104, 2012.

[10] G Aeppli and Z. Fisk. *Comment Condensated Matter Physics*, 16:155, 1992.

[11] G.E.Childs A.F.Clark and G.H. Wallace. Electical resistivity of some engineering alloys at low temperatures. *Cryogenics*, August:296–305, 1970.

[12] Patricia Lebre Alireza and Gilbert George Lonzarich. Miniature anvil cell for high-pressure measurements in a commercial superconducting quantum interference device magnetometer. *Review of Scientific Instruments*, 80(2):023906, February 2009.

[13] D. Attwood. *Soft X-Rays and Extreme Ultraviolet Radiation: Principles and Applications*. 2007.

[14] Enrico Bandiello. A study of optical propreties of crocoite (pbcro4) under cmpression. Master's thesis, Universitat de Valencia, 2011.

[15] W.A. Bassett. Diamond anvil cell, 50th birthday. *High Pressure Research*, 2:163–186, 2009.

[16] Behrens. *Trends in analytical Chemistry*, 11:218, 1992.

[17] er al Broholm. *Physical Review Letters*, 65:2063, 1990.

[18] G. Bunker. *ntroduction to XAFS: a practical guide to X-ray absorption fine structure spectroscopy*. 2010.

[19] et al C. Varma. *Physical Report*, 361:267, 2002.

[20] et al Coleman. *Journal of Physics Condensated Matter*, 13:273, 2001.

[21] R.A. Dragoset J. Chang A.R. Kishore S.A. Kotochigova C.T. Chantler, K. Olsen and D.S. Zucker. *X-ray form factor, attenuation, and scattering tables*. 2001.

[22] K.M. Purcell D.E. Graf, R.L. Stillwell and S.W. Tozer. Nonmetallic gasket and miniature plastic turnbuckle diamond anvil cell for pulsed magnetic field studies at cryogenic temperatures. *High Pressure Research: An international Journal*, 31:533–543, 2011.

[23] E.A. Stern D.E. Sayers and F.W. Lytle. New technique for investigating non crystalline structures: Fourier analysis of the extended x-rayabsorption fine structure. *Physical Review Letters*, 27:12041207, 1971.

[24] S. Doniach. *Physica B*, 91:231, 1977.

[25] R.M. Eisberg and R. Resnick. *Quantum physics of atoms, molecules, solids, nuclei, and particles*. 1985.

[26] M. I. Eremets, V. V. Struzhkin, and A. N. Utjuzh. Miniature high-pressure cells for high magnetic-field applications. *Physica B*, 211(1-4), May 1995.

[27] et al. Ermets. *Review on Scientific Instrument*, 63:3123, 1992.

[28] F.Pobell. *Matter and methods at low temperatures*. Springer, 2007.

[29] N. Funamori and T. Sato. A cubic boron nitride gasket for diamond-anvil experiments. *Review of scientific instruments*, 79, 2008.

[30] Erik Gallo. Modification of the electronic structure of catalitycally active ti metal center upon molecular adsorption: a xas/xes study. Master's thesis, Universit degli studi di Torino, 2010.

[31] A. G. Gavriliuk, A. A. Mironovich, and V. V. Struzhkin. Miniature diamond anvil cell for broad range of high pressure measurements. *Review of Scientific Instruments*, 80(4):043906, April 2009.

[32] Wojciech Gawelda. *Time-resolved x-ray absorption spectroscopy of transition metal complexes*. PhD thesis, Ecole Polytechnique Federal de Lausanne, 2006.

[33] G. Giriat, W. W. Wang, J. P. Attfield, A. D. Huxley, and K. V. Kamenev. Turnbuckle diamond anvil cell for high-pressure measurements in a superconducting quantum interference device magnetometer. *Review of Scientific Instruments*, 81(7):073905, July 2010.

[34] D.J. Griffiths. *ntroduction to quantum mechanics*. 2005.

[35] F. Groot and A. Kotani. *Core level spectroscopy of solids. Advances in condensed matter science*. 2008.

[36] A. Hofmann. *The physics of synchrotron radiation*. Cambridge monographs on particle physics, nuclear physics, and cosmology, 2004.

[37] http://xdb.lbl.gov/, editor. *X-ray data booklet*. ALS.

[38] et al J. Custer. *Nature*, 424:524, 2003.

[39] et al. Jaccarino. *Physical Review*, 160:476, 1967.

[40] J. Kondo. *Proceedings Theoretical Physics*, 28:772, 1962.

[41] J. Kondo. *Proceedings Theoretical Physics*, 32:37, 1964.

[42] D.C. Koningsberger and R. Prins. *X-ray absorption: principles, applications, techniques of EXAFS, SEXAFS, and XANES*. 1988.

[43] G. Margaritondo. *Introduction to synchrotron radiation*. 1988.

[44] S. Merkel and T. Yagi. X-ray transparent gasket for diamond anvil cell high pressure experiments. *Review of Scientific Instruments*, 76(4):046109, April 2005.

[45] Marius Millot, Sylvie George, Jean-Marc Broto, Bernard Couzinet, Jean-Claude Chervin, Alain Polian, Chrystian Power, and Jesus Gonzalez. New diamond anvil cell for optical and transport measurements under high magnetic fields up to 60t. *High Pressure Research*, 28(4):PII 906730332, 2008.

[46] E. Miranda and Dobrosavljevic V. *Report Progression Physics*, 68:2337, 2005.

[47] et al Monod. *Physical Review B*, 34:7716, 1986.

[48] et al Monthoux. *Physical Review B*, 59:14598, 1999.

[49] M. Newville. *Fundamentals of xafs*.

[50] i et al Pascarell. Energy-dispersive absorption spectroscopy for hard-x-ray micro-xas applications. *Journal of syncrotron radiation*, 13:351–358, 2006.

[51] B. Ravel. *A practical introduction to multiple scattering theory.* 2005.

[52] Smith R.D. and Keesom P.H. Specific heat of rhenium between 0.15 and 4.0 k. *Physical rewiew B*, 1(1):188–191, 1970.

[53] JJ Rehr and RC Albers. Scattering-matrix formulation of curved-wave multiple scattering theory: Application to x-ray-absorption fine structure. *Physical Review B*, 41:8139, 1990.

[54] JJ Rehr and RC Albers. Theoretical approaches to x-ray absorption fine struc- ture. *Reviews of Modern Physics*, 72:621, 2000.

[55] P. Risenbrough. *Advances in physics*, 49:257, 2000.

[56] J.J. Sakurai and S.F. Tuan. *Modern quantum mechanics. Advanced book program.* 1985.

[57] et al Scalapino. *Physical Review B*, 34:8190, 1986.

[58] J.L. Smith and P.S. Risenbrough. *Journal Magnetic Matter*, 47-48:545, 1985.

[59] F. et al. Steglich. *Physical Review Letters*, 43:1892, 1976.

[60] G. Stewart. *Review of Modern Physics*, 73:797, 2001.

[61] G. Stewart. *Review of Modern Physics*, 78:743, 2006.

[62] B.D Padalia M.N Ghatikar T.K. Hatwar, R.M. Nayak. Xray absorption spectroscopic study of mixed valence systems eucu2si2, ybcu2si2 and sm4bi3. *Solid State Communications*, 34:617–620, 1980.

[63] Yeram Sarkis Touloukian. *Specific heat, metallic elements and alloys vol.4.* 1970.

[64] M. Sigrist Tsunetsugu, H and K. Ueda. *Review of Modern Physics*, 69:809, 1997.

[65] Various. *ASM . Metal Handbook collection.* ASM international, 2004.

[66] et al von Lohneysen. Fermi liquid instabilities at magnetic quantum phase transition. *Review of Modern Physics*, 2007.

[67] G. K. White. *Landolt-Brnstein - Group III Condensed Matter - 15c.* SpringerMaterials - The Landolt-Brnstein Database.

[68] K. Cheng H.-D. Denner X. Z. Li, H. Yang and P. Cheng. Measurement of thermal conductivity of vespel sp-1 at low temperatures from 2 to 300k. *Cryogenics and refrigeration*, Proceedings of ICCR 98:545549, 1998.

[69] K. Yamamoto, S. Endo, A. Yamagishi, H. Mikami, H. Hori, and M. Date. A ceramic-type diamond anvil cell for optical measurements at high-pressure in pulsed high magnetic-fields. *Review of Scientific Instruments*, 62(12):2988–2990, December 1991.

[70] et al Y.H. Matsuda. High-magnetic-field x-ray absorption spectrscopy of field-induced valence transition in ybincu4. *Journal of thr Physical Society of Japan*, 76:034702, 2007.